MAGNETOELECTRIC HETEROJUNCTION PROPERTIES OF MULTIFERROIC MATERIALS

A THESIS SUBMITTED TO
THE GRADUATE SCHOOL OF NATURAL AND APPLIED SCIENCES
OF
MIDDLE EAST TECHNICAL UNIVERSITY

BY

ÇAĞRI ÖZDİLEK

IN PARTIAL FULFILLMENT OF THE REQUIREMENTS
FOR
THE DEGREE OF MASTER OF SCIENCE
IN
METALLURGICAL AND MATERIALS ENGINEERING

JULY 2020

Approval of the thesis:

MAGNETOELECTRIC HETEROJUNCTION PROPERTIES OF MULTIFERROIC MATERIALS

submitted by **ÇAĞRI ÖZDİLEK** in partial fulfillment of the requirements for the degree of **Master of Science** i**n Metallurgical and Materials Engineering, Middle East Technical University** by,

Prof. Dr. Halil Kalıpçılar
Dean, Graduate School of **Natural and Applied Sciences** _____

Prof. Dr. C. Hakan Gür
Head of the Department, **Metallurgical and Materials Eng.** _____

Prof. Dr. A. Macit Özenbaş
Supervisor, **Metallurgical and Materials Eng., METU** _____

Examining Committee Members:

Prof. Dr. M. Vedat Akdeniz
Metallurgical and Materials Eng., METU _____

Prof. Dr. A. Macit Özenbaş
Metallurgical and Materials Eng., METU _____

Prof. Dr. Caner Durucan
Metallurgical and Materials Eng., METU _____

Prof. Dr. Mehmet Parlak
Physics, METU _____

Assist. Prof. Dr. Yusuf Keleştemur
Metallurgical and Materials Eng., Atılım University _____

Date: 01.07.2020

I hereby declare that all information in this document has been obtained and presented in accordance with academic rules and ethical conduct. I also declare that, as required by these rules and conduct, I have fully cited and referenced all material and results that are not original to this work.

Name, Last name : Çağrı Özdilek

Signature :

ABSTRACT

MAGNETOELECTRIC HETEROJUNCTION PROPERTIES OF MULTIFERROIC MATERIALS

Özdilek, Çağrı
Master of Science, Metallurgical and Materials Engineering
Supervisor : Prof. Dr. A. Macit Özenbaş

July 2020, 74 pages

Bismuth ferrite ($BiFeO_3$) has gained a great interest over the past years as it exhibits more than one primary ferroic orders in a single phase. In the first part of this work, optimum parameters, such as reaction temperature, duration and concentration of mineralizer in the solution, for the production of bismuth ferrite particles via a hydrothermal method were determined. The second part involves the influence of Yb doping on the structural, magnetic and electrical properties of bismuth ferrite ($BiFeO_3$). Well-crystallized $BiFeO_3$ (BFO) and Yb-doped $BiFeO_3$ powders ($Bi_{1-x}Yb_xFeO_3$: x = 0, 0.01, 0.03, 0.05, 0.1) were successfully synthesized via a typical hydrothermal method. X-ray diffraction (XRD) revealed that powders have a distorted rhombohedral structure with a space group of R3c. Field emission scanning electron microscope (FESEM) studies indicated more or less cuboidal particles consisting of subparticles with different sizes. It was found that increase in Yb content retains the particle growth, therefore, reduces the size of these cuboidal particles. X-ray photoelectron spectroscopy (XPS), on the other hand, showed the presence of oxygen content in the lattice which was increased from 7.04% to 39.97% in doped $BiFeO_3$ powders, indicating that doping with Yb reduces oxygen deficiencies in the lattice and ensures the formation of more M-O-M bonds.

Vibrating sample magnetometer (VSM) measurements revealed that the highest saturation magnetization value was achieved as 0.09 emu/g for 3 at% Yb-doped BFO showing weak ferromagnetic behavior. Ferroelectric measurements were also conducted to find remanent polarization (P_r) values of samples. Among all samples, the highest P_r value, 0.37 $\mu C/cm^2$, was attained for 3 at% Yb-doped BFO. From dielectric measurements, it was proved that incorporation of Yb into $BiFeO_3$ perovskite structure enhances formation of M-O-M bonds, therefore, the highest dielectric constant and lowest dielectric loss were achieved in case of $Bi_{0.9}Yb_{0.1}FeO_3$.

Keywords: hydrothermal synthesis, multiferroic properties, bismuth ferrite

ÖZ

MULTİFERROİK MALZEMELERİN MAGNETOELEKTRİK HETEROEKLEM ÖZELLİKLERİ

Özdilek, Çağrı
Yüksek Lisans, Metalurji ve Malzeme Mühendisliği
Tez Yöneticisi: Prof. Dr. A. Macit Özenbaş

Temmuz 2020, 74 sayfa

Bizmut ferrit ($BiFeO_3$) birden fazla birincil ferroik düzeni tek bir fazda gösterdiği için son zamanlarda büyük ilgi görmektedir. Bu çalışmanın ilk bölümünde, hidrotermal yöntemle bizmut ferrit parçacıklarının üretimi için reaksiyon sıcaklığı, süresi ve çözeltideki mineralleştirici konsantrasyonu gibi optimum parametreler belirlenmiştir. İkinci bölüm, Yb katkısının bizmut ferritin ($BiFeO_3$) yapısal, manyetik ve elektriksel özellikleri üzerindeki etkisinin araştırılmasını içermektedir. İyi kristallenmiş $BiFeO_3$ (BFO) ve Yb katkılı $BiFeO_3$ tozları ($Bi_{1-x}Yb_xFeO_3$: x = 0, 0.01, 0.03, 0.05, 0.1) tipik bir hidrotermal yöntemle başarıyla sentezlenmiştir. X-ışını kırınımı (XRD), tozların R3c uzay grubuyla eğilmiş rombohedral kristal yapıya sahip olduğunu ortaya çıkarmıştır. Alan emisyonu taramalı elektron mikroskobu (FESEM) çalışmaları, farklı büyüklükteki alt parçacıklardan oluşan küboidal tip bir morfoloji göstermiştir. Yb içeriğindeki artışın parçacık büyümesini geciktirdiği, bu nedenle küboidal parçacıkların boyutunu azalttığı görülmüştür. Öte yandan, X-ışını fotoelektron spektroskopisi (XPS), kafes içindeki oksijen içeriğinin katkılı $BiFeO_3$ tozlarında % 7.04'ten % 39.97'ye yükseldiğini göstererek Yb katkılamasının yapıdaki oksijen eksikliğini azalttığını ve daha fazla M-O-M bağının oluştuğunu

belirtmektedir. Titreşimli nümune manyetometre (VSM) ölçümleri, en yüksek doygunluk manyetizasyon değerinin zayıf ferromanyetik davranış gösteren % 3 Yb katkılı BFO'da 0.09 emu/g olarak elde edildiğini ortaya koymuştur. Örneklerin kalıntı polarizasyon (P_r) değerini bulmak için ise ferroelektrik ölçümler yapılmıştır. Tüm nümuneler arasında 0.37 $\mu C/cm^2$ ile en yüksek P_r değeri % 3 Yb katkılı BFO'da elde edilmiştir. Dielektrik ölçümlerinden, Yb'nin $BiFeO_3$ perovskit yapısına dahil edilmesinin M-O-M bağlarının oluşumunu arttırdığı kanıtlanarak, en yüksek dielektrik sabiti ve en düşük dielektrik kaybı $Bi_{0.9}Yb_{0.1}FeO_3$ nümunesinde elde edilmiştir.

Anahtar Kelimeler: hidrotermal sentez, multiferroik özellikler, bizmut ferrit

Dedicated to my beloved family and Prof. James Scott referring as "father of integrated ferroelectrics", who passed away on April 6th, 2020.

ACKNOWLEDGMENTS

I would like to express my deepest gratefulness to Prof. Dr. A. Macit Özenbaş for his endless guidance and support throughout this thesis. He always shares his experience and knowledge with me. It would be impossible to complete my thesis without his advices.

I also would like to thank to Assist. Prof. Dr. Umut Adem from Izmir Institute of Technology for his assistance through ferroelectric and dielectric measurements. It was a real privilege and honor for me to share of his scientific knowledge.

It was my pleasure and honor to work with my laboratory colleagues Dr. Kerem Çağatay İçli, Dr. Mustafa Burak Coşar, Bahadır Can Kocaoğlu, Utku Er, Başar Süer, Merve Ertuğrul, Emre Burak Yurdakul. Hereby, I would like to express my special appreciation to Dr. Kerem Çağatay İçli for enlightening me about analytical thinking and broadening my perspective in science and engineering.

I am very thankful to METU Metallurgical and Materials Engineering Department for XRD, SEM and VSM studies and Central Laboratory for XPS and simultaneous DSC/TGA analyses provided during this study.

This work was supported by The Scientific Research Council of Turkey (TUBITAK) as National Grant for Priority Topics in Master Programme – 2210/C. I was indebted to TUBITAK as providing me a financial support (2224/A) to present the part of this work in 2018 MRS Fall Meeting & Exhibit, USA.

Special thanks to my colleagues Çağatay Mert Oral and Merve Çobanoğlu. I would like to thank also to Mehmet Demiroğlu, Gizem Demirkol and Yağız Küçüklergil for their sincere friendship and support in my life.

I would like to express my sincere gratitude and thanks to Ece Uslu for her endless love, support, encouragement and understandings. Whenever I need some advice I know you are always next to me.

I am indebted to my parents, Selma and Mithat, for their endless love and caring, sacrifices and supports to educate and prepare me for my future. I am so lucky that I have you in my life.

TABLE OF CONTENTS

LIST OF TABLES

TABLES

LIST OF FIGURES

FIGURES

LIST OF ABBREVIATIONS

ABBREVIATIONS	
ME	Magnetoelectric
BFO	$BiFeO_3$
XRD	X-Ray Diffraction
XAFS	X-Ray Absorption Fine Structure
SQUID	Superconducting Quantum Interference Device
DTA	Differential Thermal Analysis
DSC	Differential Scanning Analysis
DTA	Differential Thermal Analysis
SEM	Scanning Electron Microscopy
EDS	Energy Dispersive X-Ray Spectroscopy
XPS	X-Ray Photoelectron Spectroscopy
VSM	Vibrating Sample Magnetometer

CHAPTER 1

INTRODUCTION

Multiferroic materials have gained a great deal of interest as they can exhibit more than one primary ferroic property *i.e.,* ferroelectric, ferromagnetic (or even anti-), and ferroelastic ordering in a single material [1]. These type of materials enable to control electrical polarization (magnetization) under the application of magnetic (electric) field. This promising feature leads to offer a wide opportunity in the areas of spintronics [2], sensors [3], and data storage devices [4]. Among several multiferroics, numerous studies on magnetic and electrical behavior of $BiFeO_3$ (BFO) have been conducted due to its higher critical temperatures *i.e.,* Néel (T_N = 370 °C) and Curie temperature (T_C = 830 °C) [5,6], which is therefore called as a room temperature multiferroic. Also, BFO has a rhombohedrically distorted perovskite structure and belongs to R3c space group. Moreover, BFO exhibits room temperature ferroelectric and G-type antiferromagnetic behavior having a spiral modulated spin structure in the period of 64 nm [7]. Ferroelectric behavior in BFO arises from lone pair mechanism due to 6s electrons in Bi whereas magnetization originates from partially filled 3d orbital of Fe [8]. Apart from thin film or single crystal of BFO, bulk bismuth ferrites exhibit a significant leakage current due to the presence of defects or nonstoichiometric perovskite structure. Therefore, doping on Bi and/or Fe-site is generally believed to be the most effective strategy to tailor magnetoelectric properties of BFO type multiferroics.

Different methods can be used to synthesize BFO such as conventional solid state sintering [9,10], sol-gel [11,12] and hydrothermal method [13-15]. Upon formation of BFO from its precursors, Bi_2O_3 and Fe_2O_3 can easily transform into $Bi_2Fe_4O_9$ and/or $Bi_{25}FeO_{40}$ resulting in nonhomogeneous microstructure within BFO due to complex phase diagram of Bi_2O_3 - Fe_2O_3 [16]. Lower synthesis temperature at around

200 °C rather than 800 – 850 °C along with controlled phase transformation is possible in hydrothermal method without any further calcination. This leads to suppressing the decomposition of BFO, therefore, reducing the probability of the formation of secondary phases *i.e.*, $Bi_2Fe_4O_9$ and $Bi_{25}FeO_{40}$. Moreover, size and/or shape of particles can be altered by arranging concentration of mineralizers or surfactants, which in turn positively affects magnetic and ferroelectric behavior of BFO [17,18].

Several works have been reported on hydrothermal synthesis of BFO. Among them, Han *et al.* investigated effect of KOH concentration, reaction temperature and time on the mechanism of BFO formation [19]. Xu *et al.* also reported growth mechanism of BFO highlighting the influence of reactant molarity together with heating and cooling rates on the formation of crystal [20]. Moreover, Sb, Ga and Zn doping for Fe-site, rare earth elements doping (e.g. Tb, Dy, Ho) for Bi-site and co-doping of Nd and Mn/Al have been successfully utilized in BFO perovskite structure to enhance magnetoelectric properties [13-15,21-23]. Recently, Wang *et al.* reported the ferroelectric analysis of Sr, Co and co-doped BFO, speculating that remanent polarization (P_r) value of Sr-doped BFO and Co-doped BFO are 0.086 and 0.209 $\mu C/cm^2$. P-E curve shows circular loops without any saturation which may be ascribed to oxygen vacancies and unbalanced chemical state of Fe within the structure [24]. Liu *et al.* analyzed the effect of Al incorporation on 5 at% Nd-doped BFO, highlighting paramagnetic behavior without any saturation under the field of 6 T [14]. Tang *et al.* achieved the highest saturation magnetization in case of 10 at% Mn-doped BFO with a value of 0.785 emu/g. Upon further dopant addition, saturation magnetization value was decreased to 0.382 emu/g because double ion interaction might play an important role on magnetic behavior of Mn-doped BFO [25]. It is believed that employing rare earth elements in Bi site plays important role to lower leakage current present in BFO, therefore, enhancement in ferroelectric and piezoelectric properties can be achieved [26]. Since Yb^{3+} (0.0958 nm) has a smaller radius compared to Bi^{3+} (0.117 nm), a distortion within the perovskite structure becomes possible, leading to improved ferroelectric feature [27]. Ahmad *et al.*

investigated the effect of co-doped Yb and Co in BFO powders produced via wet chemical route, ending up with 0.385 emu/g as its saturation magnetization value and improvement in insulating character [28]. Lakshmi *et al.* presented a systematic study of Yb and X (X = Nb, Mn, Mo) co-doped BFO ceramics synthesized by sol-gel method, pointing out that dielectric loss could be remarkably diminished with co-doping mechanism compared to undoped BFO [29]. Among them, only Wu *et al.* analyzed doping of Yb in BFO produced by hydrothermal method in terms of photocatalytic activities, indicating that incorporation of Yb lowers the photocatalytic efficiency of BFO due to increase in energy band gap [30].

Up to now, limited attempts have been made to carry out research on Yb-doped BFO produced by hydrothermal method. Effect of Yb substitution on magnetic and electrical properties of hydrothermally synthesized BFO is still needed to be investigated. This motivates us to elucidate characteristics of Yb-doped BFOs synthesized using hydrothermal method. Therefore, in this work, single phase Yb-doped BFOs were successfully obtained at a temperature of 200 °C using stainless steel autoclave. Structural, morphological, magnetic and electrical properties of doped samples were studied in detail to understand further the multiferroic behavior of Yb-doped BFO.

CHAPTER 2

LITERATURE REVIEW

2.1 Features of Multiferroicity

Although electricity and magnetism were combined into one simple well-known equation as given by Maxwell, both are often considered in as separate way. This is because the charges of electrons and ions are responsible for electricity whereas magnetism arises from the spins of these electrons. The possibility of coupling between these two mechanisms in one material was first predicted by Pierre Curie in 1894 [31], then, Dzyaloshinskii proposed Cr_2O_3 should have a linear magnetoelectric (ME) effect based on its symmetry [32]. A year later, Astrov experimentally proved this effect in Cr_2O_3 [33]. From this development, several researches have been employed to investigate the details of magnetoelectrics in which a magnetization is proportional to applied electric field or vice versa.

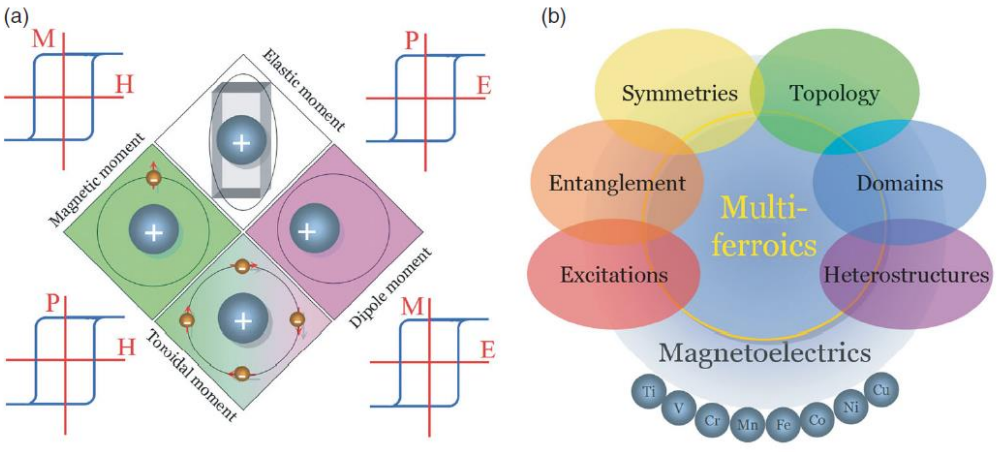

Figure 2.1. (a) Four principle ferroic orders and basis of couplings. (b) Origin of multiferroic phenomena and possible ME elements [34].

The first ‘magnetoelectric’ material, Ni-I boracite, was studied by Ascher *et al.* in 1966 [35] and later this term was coined as ‘multiferroic’ by Schmid [1]. According to his original definition, a multiferroic material includes more than one primary ferroic orders *i.e.,* ferroelectricity, ferromagnetism and ferroelasticity in a single phase as given in Figure 2.1. Nowadays, the term has gained a broader definition including anti- order in a single phase or even composite type of structure [36].

The term, multiferroic, predominantly stands for coexistence of magnetism and ferroelectricity. These type of materials enable to control electrical polarization (magnetization) under the application of magnetic (electric) field as shown in Figure 2.2. This promising feature leads to offer a wide opportunity in the areas of spintronics [2], sensors [3] and data storage devices [4]. Especially in data storage, it could be easier to write and read magnetic memory devices electrically without any current passing through, which in turn effectively reduces power consumption.

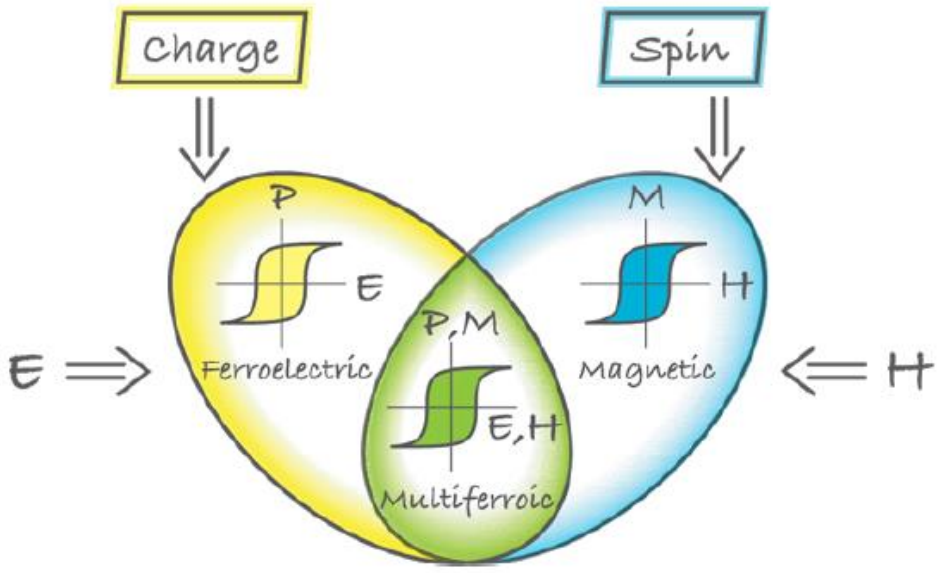

Figure 2.2. Combination of two primary ferroic orders [8].

2.1.1 Classification of Multiferroics

In a microscopic view, a magnetic material should have localized electrons, generally in the partially filled d and f shells of transition metal or rare earth ions, giving rise to a magnetic moment within the structure. The overall magnetic moments, or localized spins, govern the response of the material upon the application of magnetic field. On the other hand, there are several microscopic origins of ferroelectricity, therefore, different kinds of multiferroic materials become available. They are conceptually divided into two groups, Type-I and Type-II, based on whether magnetism induces ferroelectricity or not.

2.1.1.1 Type-I Multiferroics

Type-I multiferroics have been deeply studied up to now as they were discovered first. Both magnetic and ferroelectric ordering occur at different temperatures which are named as Néel and Curie, respectively. Generally, these type of multiferroics have a higher critical temperature as compared to that of Type-II multiferroics. For example, $YMnO_3$ has a Curie temperature at around 1000 K or Néel temperature of $BiFeO_3$ is 643 K [5,37]. They also display rather high spontaneous polarization in thin film application, *e.g.* P_s of $BiFeO_3$ ~ 100 $\mu C/cm^2$, that of $BaTiO_3$ ~ 60 $\mu C/cm^2$.

In Type-I multiferroics, both magnetism and ferroelectricity arises from two different sources *i.e.,* they are independent from one another. Presence of localized electrons results in magnetism, which are practically available in ferroelectric perovskites having Ti^{4+}, Fe^{3+}. On the other hand, ferroelectricity within the structure may result from several mechanisms as explained below correspondingly.

2.1.1.1.1 Ferroelectricity due to Lone Pairs

Existence of Bi^{3+} and Pb^{2+} ions in $BiFeO_3$ and $PbVO_3$ multiferroics brings along ferroelectricity because these type of multiferroics have two outer 6s electrons also

known as dangling bonds or lone pairs. These bonds do not participate in chemical bonding, which can be oriented into one direction for a better polarizability as shown in Figure 2.3 (b).

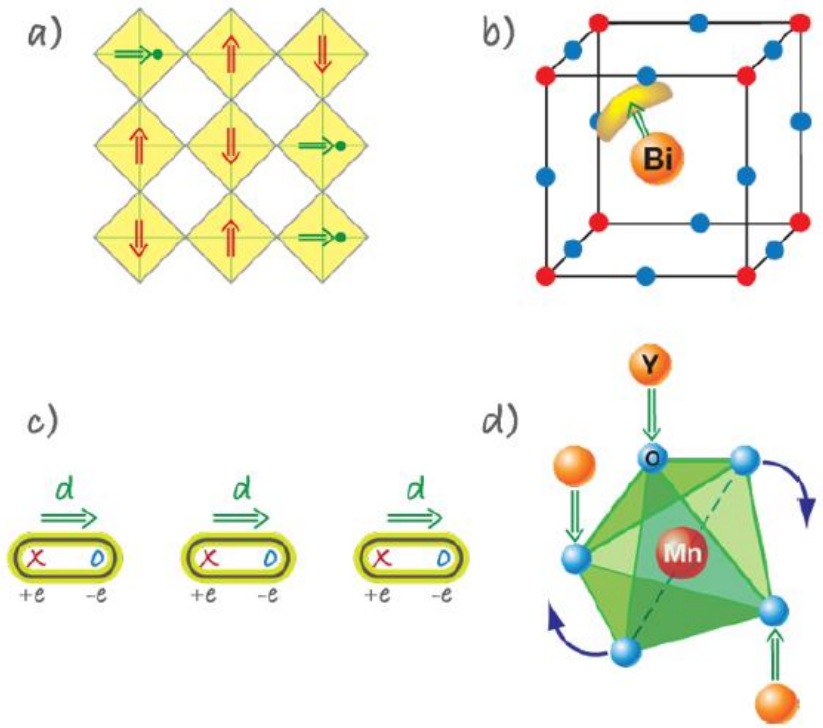

Figure 2.3. (a) Microscopic origin of multiferroics along with ferroelectrically active d^0 ions (green) and magnetic d^n ions (red). (b) Polarization of $BiFeO_3$ along [111] direction displaying ferroelectricity due to lone pair. (c) A schematic representation of ferroelectricity due to charge ordering. (d) Tilting mechanism of $YMnO_3$ as an example of geometric ferroelectricity [8].

2.1.1.1.2 Ferroelectricity due to Charge Ordering

This type of multiferroics is generally observed in transition metal compounds having different valence. In this case, both sites and bonds (long and short bonds) turn out to be imbalanced after charge ordering, as a result, ionic polarizability

becomes possible within the structure [8]. This mechanism can be valid in Ca_3CoMnO_6 [38] or $Pr_{1/2}Ca_{1/2}MnO_3$ [39]. A schematic representation of inequivalent sites can be seen in Figure 2.3 (c).

2.1.1.1.3 Geometric Ferroelectricity

The most known example for geometric ferroelectricity is $YMnO_3$ in which tilting of rigid MnO_5 block leads to a closer packing of oxygen ions towards rather small Y ions as schematically represented in Figure 2.3 (d).

2.1.1.2 Type-II Multiferroics

After the discovery of a novel type of multiferroics, a great deal of interest has been focused on the understanding of its promising feature in which ferroelectricity appears in the materials as a result of a particular type of magnetism. In other words, ferroelectric ordering is a function of magnetism and driven by the type of spin structures.

Type-II multiferroics have generally lower ordering temperatures. For instance, one of Type-II multiferroics, $TbMnO_3$ called as terbium manganite, exhibits two Néel temperatures at 41 K and 28 K where its spin structures change in between. A similar behavior was also observed in $TbMn_2O_5$ where the electrical polarization could be powerfully enhanced upon the application of magnetic field. Therefore, these type of multiferroics may open a new page for a magnetically recorded ferroelectric memory device [40].

According to types of spin structures, one can categorize Type-II multiferroics into two subgroups.

2.1.1.2.1 Spiral Type-II Multiferroics

In this type, ferroelectricity exhibits in the structure as a consequence of a particular kind of magnetic spiral. Most of the Type-II multiferroics belong to this group, which can be exemplified as $TbMnO_3$, $Ni_3V_2O_6$, $MnWO_4$ and $DyMnO_3$ [8,41]. $TbMnO_3$ displays a sinusoidal spin density wave as shown in Figure 2.4 (a) below T_{N1} (=41 K) with a zero magnetization overall, *i.e. antiferromagnetic nature*. However, magnetically active Mn ions drive the magnetic response based on non-collinear spin ordering as proposed by Dzyaloshinskii-Moriya (DM) interaction below T_{N2} (=28 K) given in Figure 2.4 (b) [42]. This interaction leads to displacement of oxygen ligands perpendicular to spin wave, hence, a non-zero polarizability (P) can become possible in the structure.

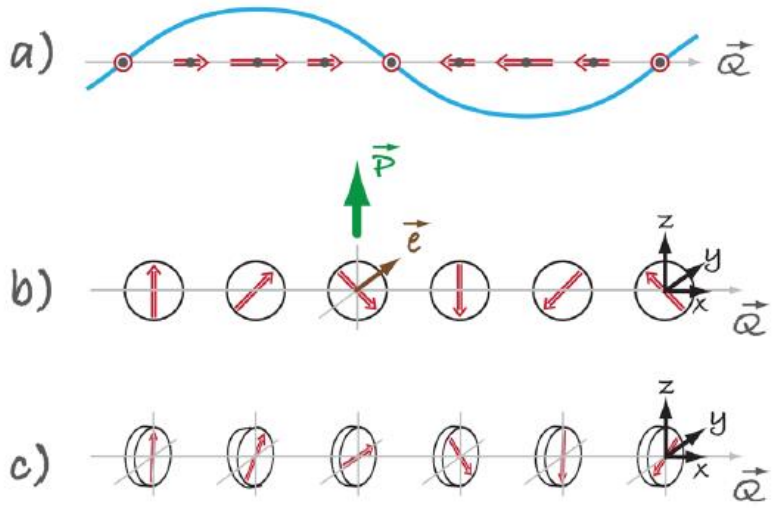

Figure 2.4. (a) A sinusoidal spin density wave with a different magnitude showing centrosymmetric structure. (b) Cycloidal spiral type of magnetism with a non-zero polarizability. (c) Proper screw type of spin structure where spins are rotating normal to wave vector (Q) [8].

In some cases as illustrated in Figure 2.4 (c), the spiral spins are rotating normal to wave vector (Q) and may produce polarizability parallel to spin propagation direction in contrast to cycloidal one. Generally, delafossite oxides AMO_2, where A

is Cu or Ag and M is a magnetic element such as Cr or Fe, display such magnetic structure. For instance, $CuFeO_2$ is one of the multiferroic materials having a proper-screw type of spin structure with an electrical polarization along its bond directions [43].

2.1.1.2.2 Type-II Multiferroics with Collinear Magnetic Structures

Besides the spin-orbit interactions in spiral type-II multiferroics, there are other certain materials that exhibit a collinear spin structure with a non-zero electrical polarizability due to breaking of inversion symmetry. In this subsection of Type-II multiferroics, all magnetic moments are aligned into a particular direction as shown in Figure 2.5. In (a), rotation of spins in a plane does not induce polarizability whereas Figure 2.5 (b) represents a similar case of cycloidal spin structure which triggers a net polarization vector (P) normal to wave vector (Q). On one hand, if one can supply an electric field toward domain walls, configuration of dipole moments may differ depending on strongness of electric field of Cu-tip as shown in Figure 2.5 (c). For example, Ca_3CoMnO_6 compound demonstrates one-dimensional chains of alternating Co^{2+} and Mn^{4+} ions where up-up-down-down spin configuration is present. This antiferromagnetic ordering breaks inversion symmetry through the exchange striction of different bonds, thus, stimulates ferroelectric polarization along the chains [38]. A similar mechanism can be also seen in the orthorhombic perovskites $RMnO_3$ where R is generally small rare earth element such as Ho, Er and Tm. In despite of presence of identical magnetic ions (Mn^{3+}) in the structure, the exchange striction results in movement of oxygen ions perpendicular to Mn-O-Mn bonds, which in turn induces electrical polarization that is generally higher than that of spin-orbit interactions [44].

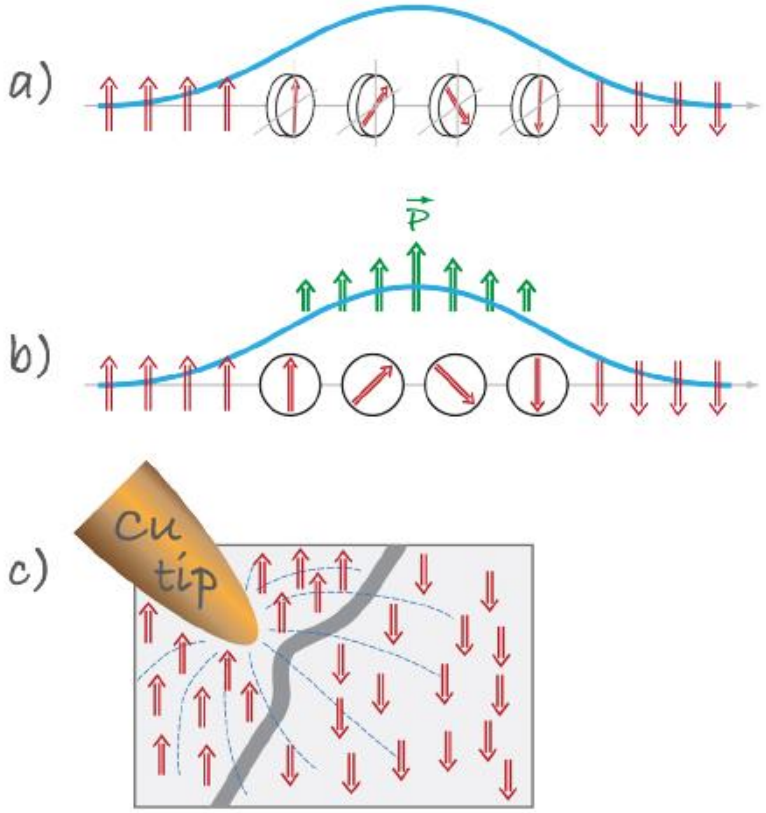

Figure 2.5. (a) Spins are rotating in a plane perpendicular to wave vector. (b) A similar case of cycloidal spiral spins producing a spontaneous polarization (P). (c) A schematic representation of effect of electric field on dipole moment configuration across Bloch walls [8].

2.2 Features of $BiFeO_3$

As aforementioned in the previous section, $BiFeO_3$ (BFO) is one of the Type-I multiferroics having a rhombohedral crystal structure. BFO has a point group of R3c with lattice parameters of a_H=5.5876 and c_H=13.867 Å in terms of hexagonal notation obtained through detailed X-ray and neutron diffraction analysis at room temperature [45]. The crystal structure of BFO could be also represented as a pseudo-cubic structure (rhombohedrally distorted perovskite) where lattice constants are given as a=3.965 Å and α=89.45° [46]. As shown in Figure 2.6 (a), Bi ions are located at the corner of unit cell whereas Fe ions are combined with O ions to form

FeO_6 octahedra. The large displacement of Bi ions relative to the octahedral gives rise to the ferroelectric state present in BFO. As the largest displacement takes place in the pseudo-cubic direction of {111}, the highest polarizability in epitaxial BFO thin films is achieved in BFO (111) case as seen in Figure 2.6 (b).

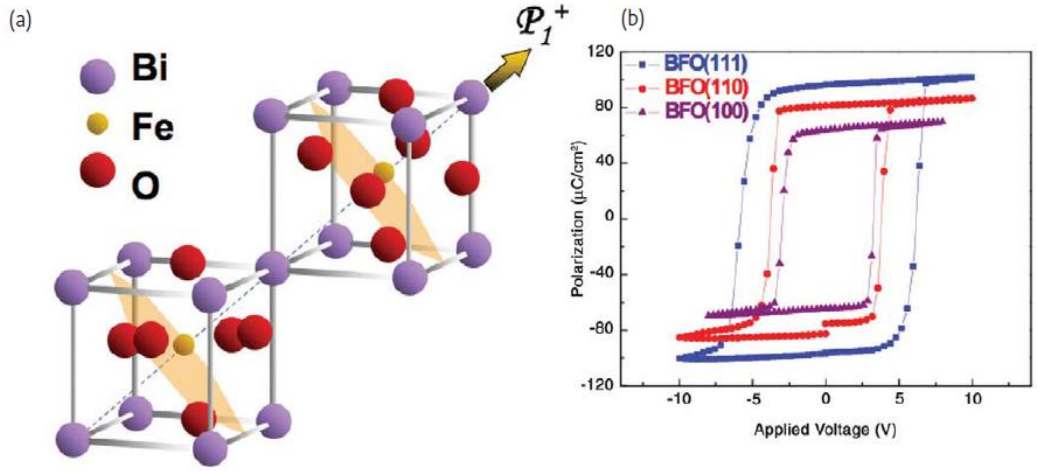

Figure 2.6. (a) A schematic representation of BFO crystal structure highlighting the highest polarization value in [111] direction. (b) Large ferroelectric polarization curves measured along [111], [110] and [100] – axis, separately [47].

Moreover, BFO displays a G-type antiferromagnetic ordering where Fe^{3+} magnetic moments are aligned oppositely between adjacent (111) planes as schematically given in Figure 2.7 (a). In fact, these spins are not perfectly antiparallel with one another, resulting in a local magnetoelectric coupling with a polarization vector (P) as schematically given in Figure 2.7 (b). In a macroscopic perspective, therefore, BFO exhibits the spin cycloid magnetic ordering in a period length of 64 nm along its propagation pseudo-cubic direction of $[10\bar{1}]$ axis as in Figure 2.7 (c). This incommensurate magnetic ordering of BFO is first proposed by Sosnowska *et al.* in 1982 where they investigated powder BFOs synthesized by a classical sintering method via a high resolution time of flight neutron diffractometer to analyze the splitting of magnetic diffraction lines of (003) and (101) [48].

As mentioned above, ferroelectricity in BFO results from dangling bonds of Bi^{3+} (*e.g.*, lone pair mechanism) along its diagonals, [111], in pseudo-cubic unit cell. To

give an example of early measurements on ferroelectricity of bulk BFO, Teague *et al.* published a paper pointing out that spontaneous polarization of bulk BFO measured along the <100> direction was 3.5 μC/cm^2 whereas 6.1 μC/cm^2 was attained along the <111> direction. This rather small polarization values might be ascribed to the leakage drawbacks due to presence of defects and/or nonstoichiometry of BFO [49]. Wang *et al.* highlighted a higher spontaneous polarization in the order of ca. 60 μC/cm^2 in heteroepitaxial thin film of BFOs grown onto single crystal $SrTiO_3$ (STO) substrates via pulsed laser deposition. The associated ferroelectric hysteresis curve is given in Figure 2.8. They came up with the fact that a slight altering of lattice parameter may profoundly affect the ferroelectric behavior of BFO [5].

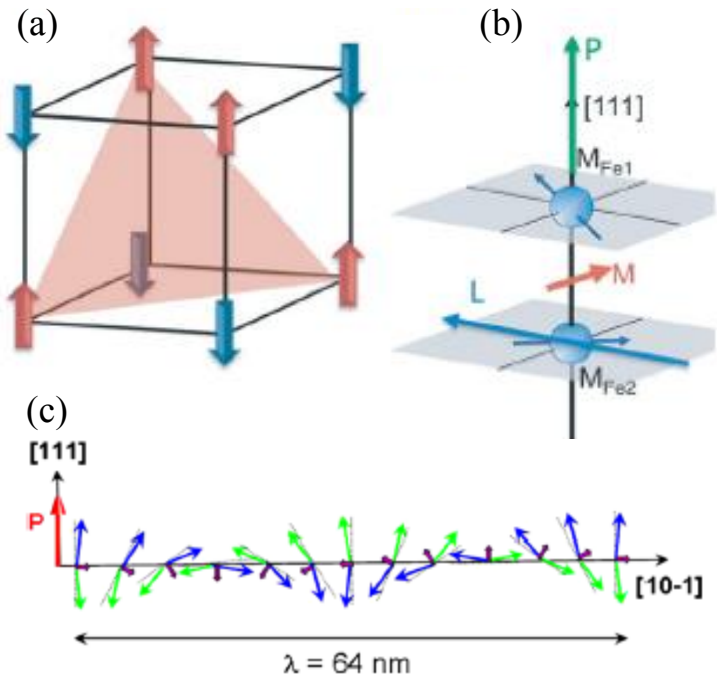

Figure 2.7. (a) A G-type antiferromagnetic nature of Fe magnetic moments within BFO. (b) A schematic representation of overall magnetic moments between consecutive planes along [111] direction in pseudo-cubic structure [50]. (c) A spin cycloid magnetic moments having a 64 nm wavelength period [51].

BFO has two distinct ferroic ordering temperatures namely Néel and Curie for magnetism and ferroelectricity. Above its Néel temperature (T_N = 643 K), antimagnetic behavior of BFO becomes paramagnetic whereas the spontaneous alignment of electric dipoles starts to vanish above the Curie temperature (T_C = 1103 K) [5], [6]. This is why BFO is also known as one of the room temperature multiferroics and the widely studied one with different forms varying from nanotubes to wires. For instance, Park *et al.* investigated the effect of size of nanopowders on magnetic properties of BFOs. In this work, these nanoparticles having a range between 15 to 100 nm were synthesized via a facile sol-gel method. The authors claimed the frustration of spin structures plays an important role on the shape of hysteresis curve and the saturation magnetization [52]. In another research, Park *et al.* successfully synthesized 1D nanotube BFOs via a template based technique where diameter of these nanotubes varies in between 240 and 300 nm with a maximum 50 μm long [53].

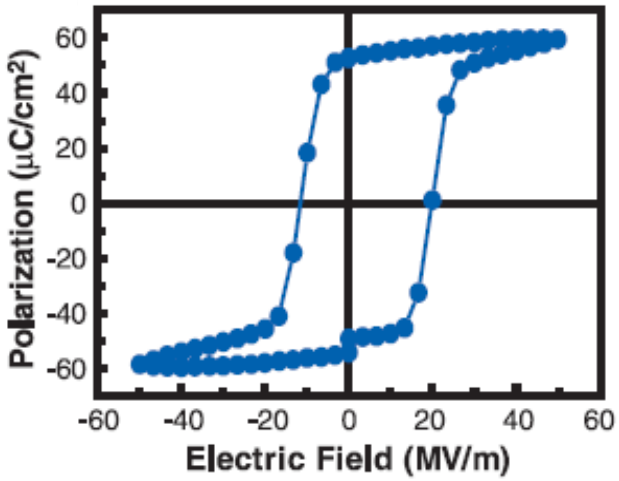

Figure 2.8. A ferroelectric hysteresis curve of epitaxial thin film BFO at a frequency of 15 kHz from Wang *et al.* work [5].

2.2.1 Phase Diagram of $BiFeO_3$

$BiFeO_3$ could be obtained using an equimolar of Bi_2O_3 and Fe_2O_3 as shown in Figure 2.9. Although BFO has been widely studied as one of the room temperature multiferroics, the detailed phase diagram was mapped out by Palai *et al.* in 2008. In this paper, numerous studies on thin film and single crystal of BFO were carried out through extensive characterization techniques, reporting that α-BFO transforms into β at around 825 ± 5 °C and β phase decomposes into γ-BFO at around 925 ± 5 °C. In the former one, an orthorhombic order-disorder tranformation takes place while cubic γ-BFO exists in the range of 925 and 933 ± 5 °C [54]. The influence of strain in the epitaxial thin film of BFO may impose a change in the crystal structure from rhombohedral phase to a modified M_A monoclinic [55], tetragonal [56], or even triclinic [57]. Different crystal structures can also be achieved via a doping mechanism [58] or solid solution formation with $BaTiO_3$ [59].

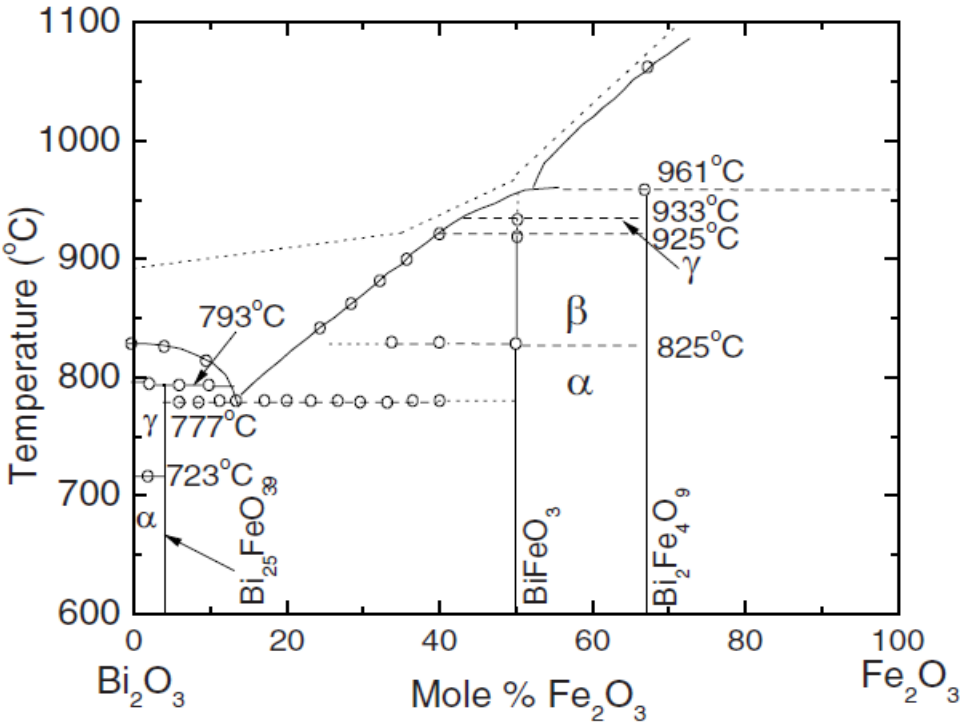

Figure 2.9. A compositional phase diagram of $BiFeO_3$ [54].

BFO is very prone to decompose into its parasitic phase, *e.g.* $Bi_{25}FeO_{39}$ and $Bi_2Fe_4O_9$, which makes difficult to synthesize pure BFO. Therefore, a controlled growth mechanism together with a careful examination of synthesis parameters become essential in the production step [60].

The important parameter in these type of perovskite structures (ABO_3) is how good the ions fit their positions, which affects their ferroic features. Furthermore, the angle of Fe-O-Fe, found as 154° to 156° in the BFO perovskite as Moreau *et al.* reported [45], may alter the magnetic ordering within the structure and the magnetic exchange interaction between the consecutive planes.

2.2.2 Synthesis Techniques of $BiFeO_3$

Preparation of single phase perovskite BFO is generally believed to be challenging as kinetic of phase formation is quite rapid and BFO is typically inclined to formation of secondary phases, *e.g.* $Bi_2Fe_4O_9$, Bi_2O_3 and/or $Bi_{25}FeO_{39}$. Leaching with nitric acid (HNO_3) may be applied to eliminate these parasitic phases after calcination of Bi and Fe precursors [61]. The main problem encountered in the BFO structures comprises of a leakage current especially in bulk form, leading to an unsaturated ferroelectric hysteresis loop. Furthermore, formation of secondary phases may have a detrimental effect on magnetic properties due to the presence of variation in Fe chemical states and increment in the concentration of oxygen vacancies that changes Fe-O-Fe angle in the perovskite.

ABO_3 type of oxides are conventionally synthesized via a solid state reaction from its precursors generally at higher reaction temperatures. The necessity of elevated reaction temperature can be overcome by a mechanical activation assisted process where a rather severe deformation is applied to the oxide precursors so as to transform oxide precursors into the desired phase [62]. There are also other ways to fabricate these functional ceramics such as sol-gel, co-precipitation, hydrothermal,

microwave, and sonochemical. These techniques are known as wet chemical methods [63].

2.2.2.1 Conventional Solid State Reaction

This method involves a consolidation of powders to form a compact body reacted in the solid state. This traditional method requires a high reaction temperature in which stoichiometric portions of A- and B- precursors are sintered in a crucible at the temperature above the eutectic point of the binary system and below the melting point, enabling the precursors to diffuse between each other. Since the diffusion and reaction take place in the solid state, a relatively long time is required in this conventional ceramic method. Decrease in surface energy drives the reaction to occur within powder particles.

The main drawback in this method includes the lack of controlled phase transformation. As Bi salts have a lower decomposition temperature compared to Fe ones, Bi_2O_3 compounds are generally found as an impurity phase in BFOs. Moreover, the secondary phases, $Bi_2Fe_4O_9$ and/or $Bi_{25}FeO_{39}$, may also be present in the final product because of a narrow region of synthesis of single phase BFO as seen in Figure 2.9. Furthermore, solid state reaction of BFO may cause a variation in the chemical state of Fe ions as a consequence of insufficient oxygen atmosphere, leading to a larger leakage current [64].

Palewicz *et al.* investigated deeply the effect of reaction temperatures on the atomic displacement of BFO synthesized via a solid state reaction method in terms of lattice parameters, Fe-O-Fe angle and Bi-Fe distance within the crystal. They reported the shift of Bi ions relative to FeO_6 octahedra as an important factor for the electrical polarization of BFO and the distance between Bi and Fe has a local maximum point near its Néel temperature [65]. On the other hand, Khomchenko *et al.* studied the effect of different dopants on the characteristics of BFO produced by a two-stage solid state method to obtain dense and single phase multiferroic [66]. In addition,

Han *et al.* proposed a new method to synthesize polycrystalline BFO thin film via solid state reaction. In their work, various calcination temperatures were tried between 500° and 800 °C for 1.5 h followed by leaching with a different molar concentration of nitric acid. In this way, they could get rid of mullite phase of BFO, $Bi_2Fe_4O_9$, with a controlled phase transformation to perform a high quality ferroelectric measurement and photovoltaic response [67]. Furthermore, Wu *et al.* gave a new insight for fabrication of single phase BFO via usual solid state method where a tartaric acid is used for a self-combustion of Bi_2O_3 and Fe_2O_3 resulting in a formation of BFO with a very short reaction time [68].

2.2.2.2 Mechanical Activation

As solid state reaction technique is taken place in a relatively prolonged time, the volatility of Bi becomes prominent, which in turn alters the stoichiometry of BFO. Formation of multi-phase structure or non-stoichiometric portion within the powders may induce a deterioration in the functional features of BFO. Therefore, a mechanically activated solid state reaction is proposed to overcome this barrier. In this method, the transformation of precursors can be expedited under the application of mechanical forces. By this way, the calcination temperature can be lowered by ca. 100° - 150 °C as compared to a classical solid state reaction. Generally, an excessive plastic deformation, *e.g.* milling operation for a various time duration, is applied for the precursor materials to initiate a reaction [63].

Maurya *et al.* compared BFO powders produced by a conventional solid state reaction and mechanical assisted technique for solid state reaction. They reported that the stoichiometric portions of Bi_2O_3 and Fe_2O_3 were treated by a high energy milling operation up to 100 h with a ball to powder ratio of 1:1. According to this work, formation of $BiFeO_3$ synthesized by a mechanical activation assisted solid state reaction is about 100 °C lower than that of solid state reaction. The reduction in grain size as a result of higher milling deformation might affect the magnetic characteristics of BFO [62]. In another study, the effect of milling energy on the

phase transformation and multiferroic properties of BFO were investigated through detailed characterization methods. They concluded the milling energy leads to decrease in leakage current in ferroelectric hysteresis measurement and lower the calcination temperature necessary for the formation of BFO [69]. The comprehensive research on the phase evaluation via this mechanosynthesis method was reported by Da Silva *et al.* with the help of ^{57}Fe Mössbauer spectroscopy. They highlighted that the core shell structure of BFO consisting of a crystalline inner core surrounded by an amorphous surface may cause an enhancement in magnetization properties. This unexpected result may be linked to the canted surface spins found in amorphous surface shell [70].

2.2.2.3 Sol-Gel Method

The sol-gel technique is the most common and versatile method for the production of functional perovskite ceramics in an economical way. 0-D, 1-D and 2-D perovskite materials can easily be synthesized with various sizes and morphologies. Depending on the treatment after gel operation, several types ranging from thin films to nano-wires, tubes, fibers can be attained as schematically given in Figure 2.10. This synthesis technique comprises of a metal source, a solvent and a chelation agent, as starting agents of the chemical reaction. Ordinarily, metal nitrates or chlorides are taken as a metal source instead of metal alkoxides due to their abundancy. The organic solvents used in sol-gel method are generally 2-methoxyethanol (2-MOE) and ethylene glycol (EG) as they have good solubility in water and a tendency to form a continuous and stable polymer molecule. Furthermore, the selection of chelation agent is of interest because it initiates the gelation process under certain conditions, thereby plays a crucial role in phase morphology of the end product. Acetic anhydride, acetic acid, citric acid or tartaric acid are the general examples of chelation agents.

A typical sol-gel method includes a hydrolysis process from a colloidal system including a metal source and a solvent. The prepared chemical solution is generally

exposed to heating operation, which transforms then into a cross-linked polymer called as “gel” along with evaporation of solvent. The amorphous “gel” is then subjected to a post-heat treatment to form a crystallized powder at elevated temperature. Dispersion of solid particles in the colloid, duration of heat treatment, selection of chelating agent are the most important parameters in this subclass of wet chemical method, influencing the homogeneity and size distribution of powders [71].

Park *et al.* employed a sol-gel method using ethylene glycol for the production of single phase BFOs in a various size range. In this study, the canting of spin moments were analyzed in detail to understand its effect on magnetic characteristic of BFO. It was stated that reduction in the period length of spiral modulated spin structure enhances the saturation magnetization value as compared to bulk BFO, verifying with superconducting quantum interference device (SQUID) and Mössbauer measurements [52]. In another work, Chen *et al.* synthesized single phase BFOs by dissolving precursor materials in acetic acid and 2-methoxyethanol with an excess Bi-nitrate to compensate the volatility of Bi during sintering at 450 °C. The ferroelectric measurement showed a saturation loop at 180 kV/cm with a remanent polarization value of 56 $\mu C/cm^2$ ($=2P_r$) as shown in Figure 2.11 even though the leakage current of ceramic samples is $3.02x10^{-4}$ A/cm^2 at 119 kV/cm just before the breakdown voltage. Weak ferromagnetism was found in the samples having a remanent magnetization value of $1.5x10^{-5}$ μ_B/Fe measured via SQUID [72]. In Liu *et al.* paper, they demonstrated a modified sol-gel method with polyvinyl alcohol (PVA) to synthesize pure BFOs. PVA acts as a complexing agent, in other words, it behaves as a coordinating polymer to metal cations with the aim of formation of fully cross-linked chains in the sol. Depending on the ratio of metal ions to OH^-, fabrication of pure BFO could be possible without any secondary phases [73].

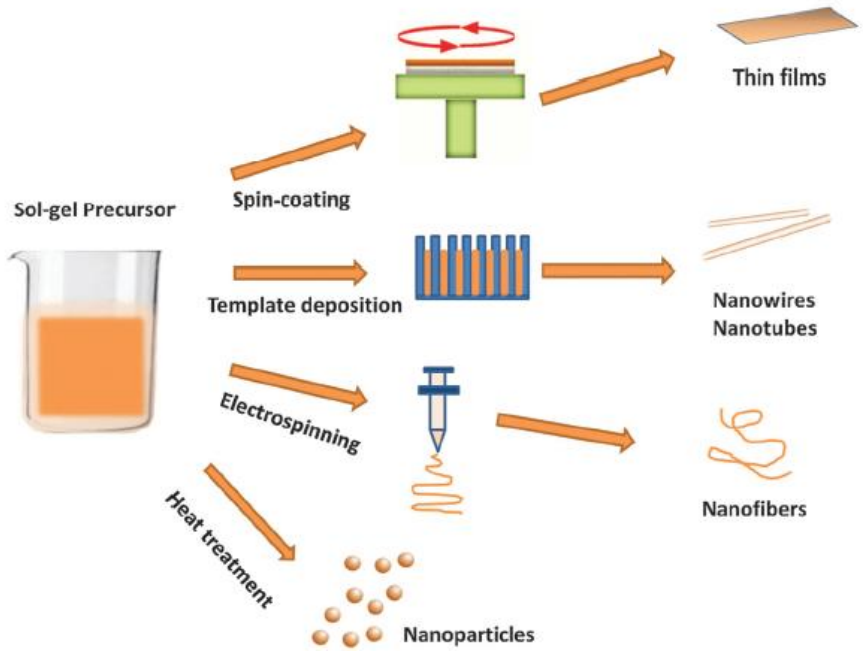

Figure 2.10. Different preparation techniques in sol-gel method [74].

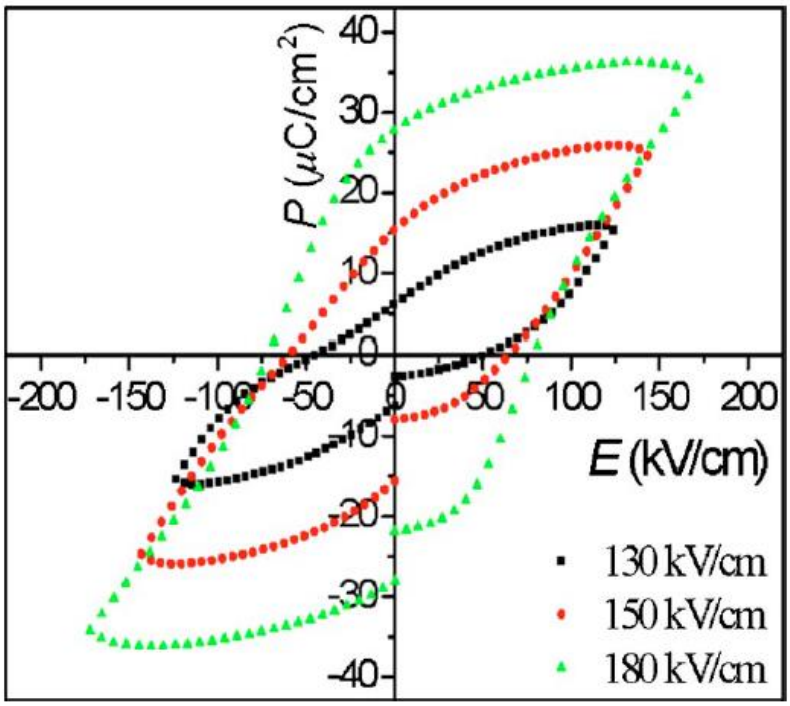

Figure 2.11. Ferroelectric hysteresis curves of BFO under different applied voltages [72].

2.2.2.4 Sonochemical Method

Ultrasound waves are used to initiate the reaction between the particles dissolved in the liquid. This method does not include any high reaction temperature, high pressure or any long heat treatment from the outside. On the contrary, these kind of waves can provide an excessive amount of energy in the localized hot spot region within the liquid having a temperature above 5000 °C, a pressure of 500 atm approximately. This rather unique feature of ultrasound wave enables to employ in high energy chemistry through a serial process, the formation, growth and implosive collapse of bubbles in the liquid [75]. Generally, the wavelength of the applied ultrasound waves are roughly ranged from 10 cm to 100 μm, in other words, their frequency range is varied in between 20 kHz and 15 MHz. As the wavelength of ultrasound waves is comparable with the molecular size, it provides a powerful tool in the production of nanostructured materials [76].

To give an example of this method in BFO synthesis, Mazumder *et al.* investigated the effect of particle size on the Néel temperature in a comprehensive way. Bulk samples were prepared via a conventional co-precipitation method whilst finer samples having a range of 4 to 50 nm were produced through sonochemical and solution evaporation techniques. A small addition of decalin was also used in the sonochemical method to give a durable power transfer in the mixed aqueous solution of Bi and Fe nitrate. After drying operation in the vacuum oven at 40 °C, samples were examined by SQUID magnetometer in order to understand the behavior of glassy state at around 100 K [77]. In another research of Das *et al.* proposing a route for the production of BFO via a sonochemical and micro-emulsion method, PEG 400 was added into bismuth and iron nitrates solution to increase the surface area of particles and decalin was used for the same purpose as in previous work. The obtained precipitation washed with distilled water was then calcined at 500 °C to attain a single phase bismuth ferrite [78].

2.2.2.5 Hydrothermal Method

Hydrothermal method may be the most versatile synthesis technique for various inorganic ceramics which are hard to obtain without any appearance of secondary phases especially through a traditional solid state reaction. Unlike solvothermal method whose liquid media is non-aqueous solution, distilled water is generally the main solvent in the dissolution of precursor materials in hydrothermal synthesis. The main advantage of this method among the others is to offer a quite lower reaction temperature in the range of 180 to 220 °C, as compared to a solid state sintering or a sol-gel method, resulting from an enclosed region in the sealed vessel. This enclosed region promotes an autogeneous pressure within the sealed vessel (also named as autoclave, bomb), exceeding the ambient pressure without any evaporation of solvent. As the reactivity of precursors takes place in the solutions by means of ions and/or molecules instead of diffusion at the interface of the powders in solid state method, the reaction becomes faster in this method [79].

A typical synthesis of BFO via a hydrothermal method includes a dissolution of Bi and Fe nitrates in deionized (DI) water and/or nitric acid (HNO_3). Hydroxide mineralizers (KOH, NaOH) are usually added to the solution in the purpose of controlling the crystallite size of end product. The prepared solution containing $Fe(OH)_3$ and $Bi(OH)_3$ is then transferred into a Teflon lined autoclave to drive the reaction during the hydrothermal stage [74]. The size and shape of the particles can be tuned with the help of several key factors. For instance, temperature plays an important role in the successful composition of BFO from its hydroxides and may alter the size and shape of nanoparticles. Moreover, the radius of cation ions in the mineralizer and pH of the solution also affect the morphology and single phase formation in the hydrothermal method. Furthermore, the molar concentration of the precursors is of importance because it changes the status of supersaturated solution in the vessel [80]. Therefore, this technique provides an opportunity to synthesize BFO powders having a narrow size distribution and desired morphology under these factors. The main disadvantage is on the other hand that extremely harsh reaction

conditions make inconvenient to perform in-situ analysis for the understanding of crystal growth.

Chen *et al.* reported a comprehensive analysis on the BFO fabrication via a hydrothermal method in terms of mineralizer concentration, duration and temperature of the reaction. KOH was used as a mineralizer in different molarity ranging from 4 M to 10 M, stating that higher KOH concentration favors the irregular shape of crystallites and formation of secondary phases. Moreover, temperature above 200 °C is required to form single phase BFO, however, below this point presence of secondary phases, $Bi_{25}FeO_{40}$ and $Bi_2Fe_4O_9$, is also favored along with $BiFeO_3$ as given in Figure 2.12. On the other hand, the duration of reaction does not significantly affect the phase evolution if the molarity of mineralizer and temperature are adjusted correctly [81]. In another work, various morphologies of BFO such as microsphere, micro-octahedron, truncated cube were obtained in different molarity of KOH mineralizer. Variation in surface energy of the particles leads to favor anisotropic growth under particular KOH concentration. At lower molarity, the surface energy of BFO particles does not vary much, as a result, more or less spheres are obtained. However, higher in KOH concentration triggers the variation in the surface energy of particles to agglomerate distinctively. The corresponding BFO evolution from its nuclei are schematically illustrated in Figure 2.13. In addition, the effect of morphology on the magnetic, electrical and optical properties are also discussed in this work in detail [82]. Han *et al.* reported that the synthesis of single phase BFO is strongly correlated with the pH of solution. Adjustment of pH approximately in the range of 14 and addition of a small amount of H_2O_2 ease the fabrication of BFO without any by-product [83]. In the work of Li *et al.*, single phase BFO was synthesized with the additions of nitric acid and PEG – 2000 as distinct from its normal hydrothermal route. Since BFO displays a narrow band gap about 2.2 eV with uniform morphology, it may be useful in photocatalytic and visible range applications [84].

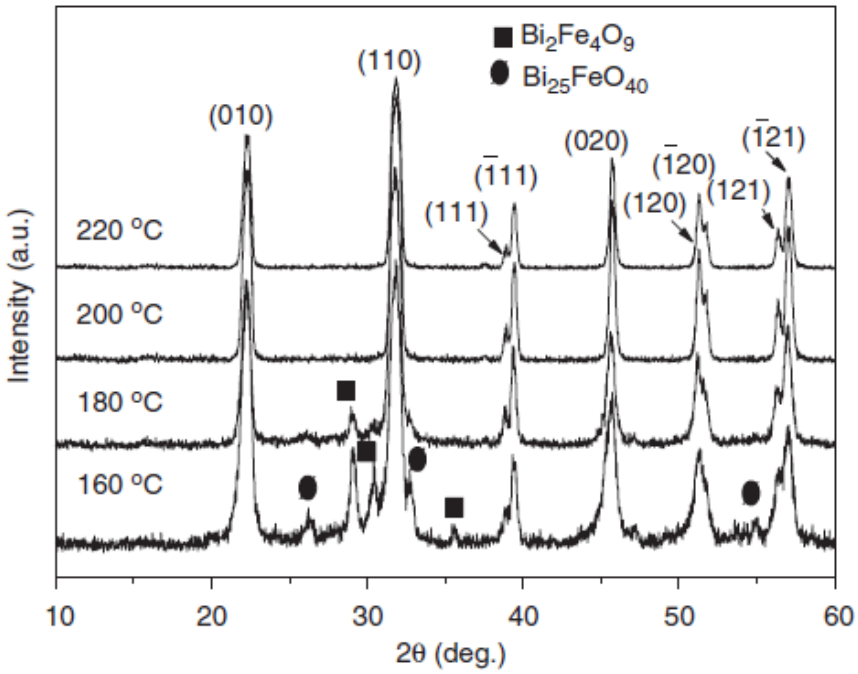

Figure 2.12. XRD pattern of BFO series under different reaction temperatures using 4 M KOH concentration and 6 h duration [81].

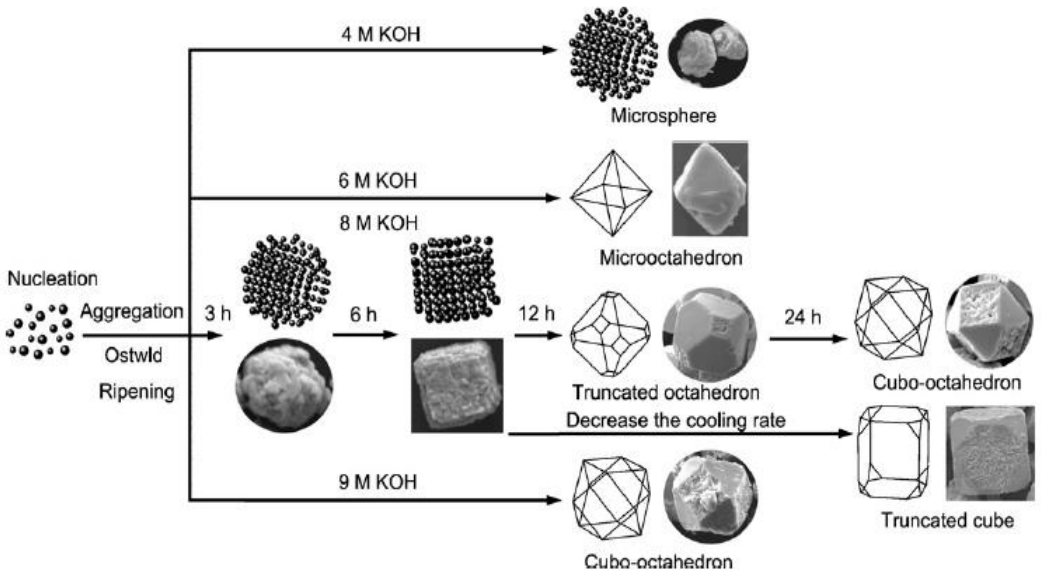

Figure 2.13. A schematic illustration of formation mechanism of BFO under different molar concentration [82].

2.2.2.6 Microwave and Microwave-Assisted Hydrothermal Method

Microwave synthesis includes an interaction of electromagnetic radiation having a higher frequency with permanent dipole moment of molecules in the solution. Since hydrothermal method provides a narrow size distribution of powders with higher crystallinity and purity under low reaction temperature, combination of microwave and hydrothermal methods offers a rapid and convenient method for the crystal nucleation and growth mechanism in a molecular way. The main advantage of microwave-assisted hydrothermal method compared to a traditional hydrothermal one is to lower reaction time significantly.

Gonjal *et al.* compared BFOs produced by three main methods, hydrothermal, microwave and microwave assisted hydrothermal, in terms of purity. As BFO crystallites formed within 30 min and at a moderate temperature of about 200 °C, the last technique offers a convenient way for the fabrication of BFO [85]. Joshi *et al.* synthesized BFOs through a microwave method where nanocubes in the range between 50-200 nm were successfully produced by a microwave reaction taken place at 180 °C for 30 min. Photoinduced oxidation may enable BFO to employ as a photoelectrode and/or photocatalytic material due to narrow size band gap [86]. Zhu *et al.* published a paper about synthesis of two distinct bismuth ferrites, spherical $BiFeO_3$ having a range of 10-50 nm and hexagonal shape of $Bi_{12}Fe_{0.63}O_{18.945}$ having a range of 18-33 nm, via a microwave-assisted hydrothermal method at 180 °C for 1 h. Due to a smaller size of particles and presence of unique hexagonal shape, the sillenite- type bismuth ferrite may be used as a promising photocatalytic material in the visible light region [87].

2.2.3 Ion Substitution in BFO

Doping plays a significant role on the ferroelectric and magnetic features of BFO by ion substitution at either Bi or Fe site, or even at both sites. This substitution may tailor the angle and distance between M-O-M bonds in the perovskite structure or

create lattice distortion, leading to change in the magnetic, electrical and optical properties in BFO.

2.2.3.1 Substitution for Bi Site

Since Bi ions are responsible for ferroelectricity due to dangling bonds, addition of dopant on the Bi site strongly affects electrical properties of BFO. Different elements are employed to enhance this property and some of them are tabulated in Table 2.1.

Wang *et al.* investigated the effect of Nd doping on Bi site in terms of structural and magnetic characteristics of BFO using XRD, XAFS, and SQUID. Nd-doped BFOs are synthesized via a conventional hydrothermal method in 4 M KOH concentration at 200 °C for 4 h. Substitution of Nd with Bi does not create any phase change or secondary phase, therefore, all samples are indexed as a rhombohedral structure having a space group of R3c. On the other hand, presence of ferromagnetic behavior in 4% Nd-doped BFO is attributed to nano-phase separation (R3c and Pnma) as confirmed via a XAFS technique [13]. In another work of Lu *et al.*, Sb-doped BFOs were synthesized via a hydrothermal route at 200 °C for 6 h with a molar concentration of 10 M in KOH solution. A large and saturated ferroelectric loop was observed in 1% Sb-doped BFO having a remanent polarization value of 40 $\mu C/cm^2$ at a frequency of 1.67 kHz as a result of pinning effect [15]. Effect of Ba dopant on the structural and magnetic properties of BFO was examined by Makhdoom *et al.* where polycrystalline Ba-doped BFOs were synthesized via a conventional solid state reaction at around 800 °C for 20 h with the help of milling operation for 30 min. Saturation and remanent magnetization was clearly increased to 0.85 emu/g with the addition of Ba into Bi sites, which is attributed to suppressing of spiral spin structure [88]. Yan *et al.* prepared Yb-doped BFOs fabricated through a rapid liquid phase sintering where ball milled powders were subjected to calcination at around 855 °C. Addition of Yb into perovskite structure induced a lattice distortion and the largest strain was observed in case of $Bi_{0.85}Yb_{0.15}FeO_3$. Due to the oxygen vacancies and motion, leakage current was observed in the samples, reaching its lowest value of

5×10^{-5} A/cm^2 in BFO – 15 % Yb. Ferroelectric measurements revealed that undoped BFO and BFO- 15%Yb have a remanent polarization value of 2.1 and 8.5 μC/cm^2 in the field of 100 kV/cm, respectively [27]. Sm, Y and La elements are also used to improve multiferroic properties of BFO and the detailed information corresponding to these studies are given in Table 2.1.

Table 2.1 Ion substitution at Bi site and its effects in terms of structural, electrical and magnetic properties.

Dopant	*Method*	*Structure*	P_r *(μC/cm^2)*	M_s *(emu/g)*	*Ref.*
Nd	hydrothermal	rhombohedral	-	0.4-1.2	[13]
Sb	hydrothermal	rhombohedral	40-45	-	[15]
Ba	solid state	rhombohedral	-	0.07-0.85	[88]
Yb	liquid phase sintering	rhombohedral	2.1-8.5	-	[27]
Yb	solid state	rhombohedral	24.3-41.5	-	[89]
Sm	solid state	rhombohedral	10.5-28.0	0.15	[10]
Y	solid state	rhombohedral - orthorhombic	-	0.121-0.467	[9]
La	sol-gel	rhombohedral	-	-	[90]

2.2.3.2 Substitution for Fe Site

As magnetically active Fe ions are responsible for magnetic behavior in BFO, substitution of Fe with another element may tailor the crystal structure and magnetism within the perovskite. Table 2.2 lists doped BFO in Fe site in terms of synthesis method, crystal structure, remanent polarization and saturation magnetization of the selected studies.

In the work of Arora *et al.*, non-magnetic Zr^{4+} ions were used to substitute Fe ions through a traditional sol-gel method calcinated at 550 °C for 2 h. Addition of Zr did

not change the crystal structure of BFO, hence, all peaks were indexed to a rhombohedral structure without showing any parasitic phases. Reduction in spiral spin moments and a structural distortion induced by Zr substitution led to a larger saturation magnetization in Zr-doped samples [91]. In another work of Khajonrit *et al.*, $BiFe_{1-x}Ni_xO_3$ nanoparticles were fabricated via a sol-gel method sintered at 600 °C for 3 h at a heating rate of 10 °C min^{-1}. Ni addition results in a formation of secondary phase, $Bi_2Fe_4O_9$ and $NiFe_2O_4$. X-ray absorption near edge spectra (XANES) revealed that Ni^{2+} substitutes Fe^{3+} ions having a larger ionic radius. The highest saturation magnetization value was obtained in case of 3 at % Ni-doped sample at room temperature under the application of 3 T [92]. On the other hand, doping with Mn in BFO caused a change in the crystal structure from rhombohedral to orthorhombic and in the magnetic behavior from antiferromagnetic to ferromagnetic having the highest saturation magnetization value of 2.75 emu/g at 10 K under the application of 2 T [93]. Cr, Ti, Co, Nb and Ho are also used to enhance magnetic nature of BFO as given in Table 2.2 with their related results.

Table 2.2 Ion substitution at Fe site and its effects in terms of structural, electrical and magnetic properties.

Dopant	*Method*	*Structure*	P_r ($\mu C/cm^2$)	M_s (*emu/g*)	*Ref.*
Zr	sol-gel	rhombohedral	-	0.44-9.33	[91]
Ni	sol-gel	rhombohedral with secondary phases	-	0.51-19.12	[92]
Mn	hydrothermal	orthorhombic	-	0.0027-2.75	[93]
Cr	hydrothermal	rhombohedral	-	0.263-0.502	[94]
Ti	solid state	rhombohedral	0.081	0.1	[95]
Co	sol-gel	rhombohedral with secondary phase	-	1.6	[96]
Nb	solid state	-	0.15	0.3-0.9	[97]
Ho	solid state	rhombohedral	5.4-8.4	0.0258-0.364	[98]

2.2.3.3 Substitution for both Bi and Fe Sites

There are also various papers to investigate the influence of substitution for both Bi and Fe sites of BFO in terms of structural and multiferroic properties. As Bi ions drive the ferroelectric behavior of BFO and magnetism is induced by magnetically active Fe ions, a proper replacement in both sites may give the optimum solution in multiferroic BFO. Some of these attempts are tabulated in Table 2.3.

Table 2.3 Ion substitution at both sites and its effects in terms of structural, electrical and magnetic properties.

Dopant	*Method*	*Structure*	P_r $(\mu C/cm^2)$	M_s *(emu/g)*	*Ref.*
Gd-Mn	hydrothermal	rhombohedral - orthorhombic	0.085	1.12	[99]
La-Mg	solid state	rhombohedral	-	-	[100]
Pr-Ti	solid state	rhombohedral - orthorhombic	-	0.75-0.9	[101]
Gd-Ti	solid state	rhombohedral - orthorhombic	-	0.1-0.2	[102]
Ho-Ni	solid state	rhombohedral	-	0.4	[103]
Y-Zr	solid state	rhombohedral	0.09-0.21	0.6-1.5	[104]
Ba-Ni	sol-gel	rhombohedral - tetragonal	0.63	2.3	[105]
La-Zr	solid state	rhombohedral	-	0.125	[106]

The highest saturation magnetization among these studies was obtained with the addition of Y and Zr in both sites where co-doped powders were ball milled for 24 h and then synthesized via a conventional solid state reaction at 800 – 840 °C for 1 h. Dopants did not induce any phase transition as there was no peak split in XRD spectrum. The replacement of Fe^{3+} with Zr^{4+} having a different valence and radius

perturbed the spiral spin structure in the perovskite BFO, strenghening the Fe-O-Zr bond [104]. In another work, substitution of Gd and Mn in both sites led to change in crystal structure from rhombohedral to orthorhombic state. P-E curves exhibited a round shape indicating the significant leakage current in doped BFOs [99]. In Castaneda *et al.* work, Ba and Ni were added into multiferroic BFO in Bi and Fe sites via a modified sol-gel method, respectively. The remanent polarization and saturation magnetization values were found as 0.63 $\mu C/cm^2$ and 2.3 emu/g [105]. Substitution of La, Pr, Ho for Bi site and Mg, Ti, Ni and Zr for Fe site are also employed in BFO and the detailed multiferroic properties can be seen in Table 2.3.

CHAPTER 3

EXPERIMENTAL PART

This work consists of two main parts, finding an optimum way for pure BFO synthesis without any secondary phases and doping with Yb to enhance multiferroic properties of BFO. For this purpose, various reaction temperatures, durations and KOH concentrations were applied to obtain the optimum process parameters. After that, Yb-doped BFO powders were synthesized and their structural, ferroelectric and magnetic characteristics were investigated.

3.1 Synthesis of BFO and Yb-doped BFO

Prior to hydrothermal method, bismuth nitrate (Sigma-Aldrich, >99.99% $Bi(NO_3)_3.5H_2O$) and iron nitrate (Sigma-Aldrich, >99.99% $Fe(NO_3)_3.9H_2O$) powders were mixed in a crucible and reacted in the solid state. The solid state reaction was conducted via in situ X-ray diffractometer (XRD) (Rigaku D/MAX 2200) and in a simultaneously taken differential scanning calorimeter (DSC), thermogravimetric (TGA) and differential thermal analysis (DTA) (SDT 650) to understand the crystal formation of bismuth ferrite.

On the other hand, in a typical hydrothermal procedure for formation of BFO and Yb-doped BFO ($Bi_{1-x}Yb_xFeO_3$: x = 0, 0.01, 0.03, 0.05, 0.1) particles, bismuth nitrate (Sigma-Aldrich, >99.99% $Bi(NO_3)_3.5H_2O$), iron nitrate (Sigma-Aldrich, >99.99% $Fe(NO_3)_3.9H_2O$), ytterbium nitrate (Sigma-Aldrich, >99.9% $Yb(NO_3)_3.5H_2O$) and potassium hydroxide pellets (Merck, KOH) were used as the starting chemical reagents. The names of samples were abbreviated according to their atomic percentage of dopant *e.g.,* BYb3FO stands for $Bi_{0.97}Yb_{0.03.}FeO_3$. Detailed abbreviations of the samples are given in Table 3.1. All these ingredients were of analytical grade purity and used as received without any further purification. To

understand the synthesis parameters on the formation of bismuth ferrite, reaction duration (5, 10 and 20 h), temperature (175, 200 and 225 °C) and KOH concentration in the solution (4, 8 and 12 M) were varied individually.

Table 3.1 Abbreviation of the samples.

Sample	*Percentage of dopant (at %)*	*Chemical Formula*
BFO	0	$BiFeO_3$
BYb1FO	1	$Bi_{0.99}Yb_{0.01}FeO_3$
BYb3FO	3	$Bi_{0.97}Yb_{0.03}FeO_3$
BYb5FO	5	$Bi_{0.95}Yb_{0.05}FeO_3$
BYb10FO	10	$Bi_{0.9}Yb_{0.1}FeO_3$

Figure 3.1. Hydrothermal set-up for synthesis of BFO and Yb-doped BFO.

Typically, stoichiometric amount of bismuth, iron and ytterbium nitrate were dissolved in 40 mL of 8M KOH with a constant magnetic stirring. After obtaining brownish color, the mixture was directly transferred into stainless steel autoclave (Amar Equipments) to perform hydrothermal treatment as seen in Figure 3.1. Hydrothermal synthesis was carried out at a reaction temperature of 200 °C for 10 h under autogeneous pressure. After cooling down to room temperature naturally, the produced powders were collected from the bottom of autoclave and centrifuged (Hettich Universal 320) several times with deionized water to get rid of K^+ and OH^- ions. Finally, obtained powders were dried at 85 °C for 6 h in a drying oven (Memmert). All these steps and parts of procedure are summarized in Figure 3.2. To measure the electrical properties of all samples, powders were pelletized by a hydraulic press (Hisan) with a diameter of 13 mm and a thickness of 1 mm.

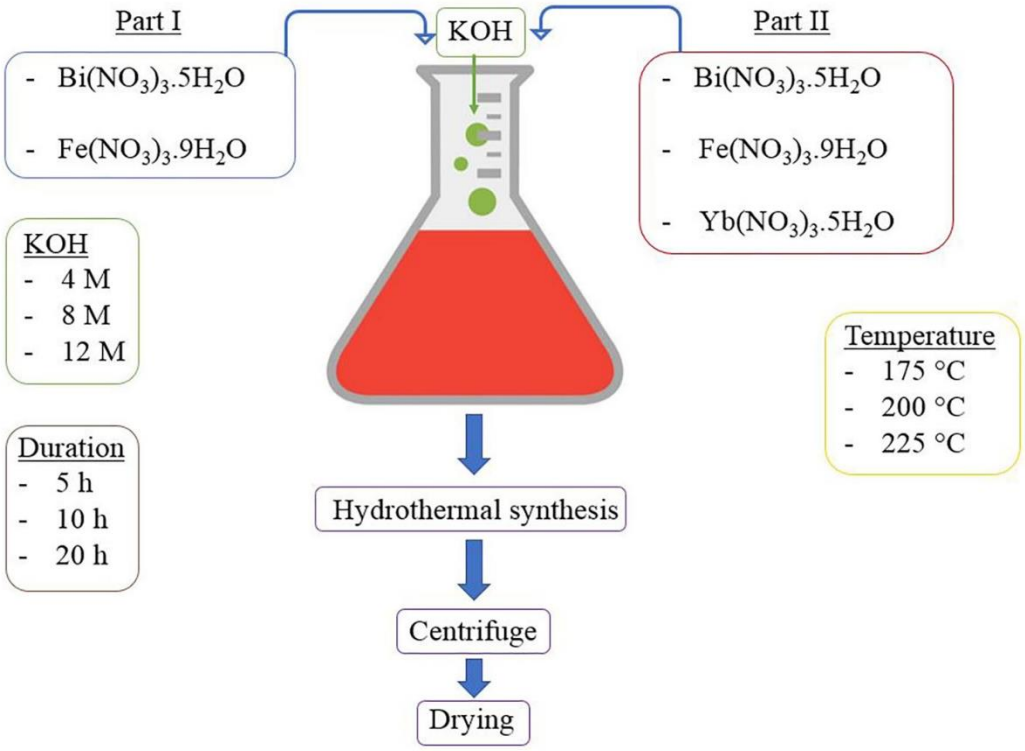

Figure 3.2. The experimental procedure of this study highlighting all the applied steps.

3.2 Characterization of the Samples

Crystalline structures of synthesized powders were investigated via an X-ray diffractometer (XRD) (Rigaku D/MAX 2200) using monochromatic Cu Kα radiation operated at 40 kV and 30 mA. Diffraction patterns for all samples were collected with a scanning rate of 0.05 °/min in 2θ range of 20-80 °. The particle size and morphology of powders were characterized by a scanning electron microscopy (FEI Quanta 400 FEG equipped with EDX analyzer). To eliminate charge build up on particle surfaces, powders were coated, before SEM operation, with a thin layer of gold nanoparticles with the help of Quorum SC7640 sputter coater. Thermal properties of BFO and Yb-doped BFOs were attained using simultaneous thermogravimetry (TGA) and differential scanning calorimeter (DSC) analysis (SDT 650), which was performed from 200 °C to 950 °C in nitrogen ambient at a scan rate of 10 °C/min. Chemical analysis of powders were conducted using X-ray photoelectron spectroscopy (XPS) (PHI 5000 VersaProbe) with a monochromatic Al Kα source. Ferroelectric hysteresis loop for undoped and Yb-doped BFO series was obtained using ferroelectric test system (Aixact TF Analyzer 1000) at a frequency of 10 Hz under the applied voltage of 50 kV/cm. In addition, dielectric measurements of all samples were performed using the same test system (Aixact TF Analyzer 1000) as a function of frequency ranging from 20 Hz to 300 kHz at room temperature. Finally, magnetic properties of powders were attained using vibrating sample magnetometer (ADE Magnetics EV/9 Model) as a function of applied magnetic field in the range of ± 10000 Oe (1 T).

CHAPTER 4

RESULTS AND DISCUSSION

As given in Chapter 3, the first part of this study includes a comprehensive analysis on how process parameters in hydrothermal method influences the evolution of bismuth ferrite crystallites. After understanding the phase evolution and obtaining the optimum parameters, the second parts involves the investigation of Yb-doped bismuth ferrites in terms of structural and their multiferroic features.

4.1 Effect of Synthesis Parameters on BFO Crystallites

As a preliminary study, the solid state reaction of bismuth ferrite was conducted to understand the phase evolution. First of all, in-situ XRD starting from 25 °C to 900 °C and simultaneous DTA-TGA-DSC analysis in the range of 200 °C to 950 °C at a scan rate of 10 °C/min were performed. As shown in Figure 4.1, below 200 °C, Bi_2O_3 (JCPDS No. 75-4627) and Fe_2O_3 (JCPDS No. 01-1053) react to form perovskite BFO. Nucleation of BFO starts quickly at around 200 °C and completes its transformation at around 750 °C as seen in Figure 4.2. All the major peaks can be indexed to a single phase BFO (JCPDS No. 86-1518). After this point, there is no significant change in BFO peaks and non-stoichiometric portion of Bi and Fe oxides and non-controlled solid state reaction lead to development of secondary phases of BFO, namely $Bi_{25}FeO_{40}$ (JCPDS No. 73-9538) and $Bi_2Fe_4O_9$ (JCPDS No. 25-0090). The obtained powders were then cooled from 900 °C to 25 °C and XRD pattern taken at room temperature is given in Figure 4.3.

In thermal analysis of BFO, Figure 4.4 shows a dramatic decrease up to 200 °C in the weight percent loss of 64%. This huge loss corresponds to decomposition of nitrates and evaporation of water. After this point, nucleation of BFO crystals starts to form and it almost completes its transformation at around 600 °C. DSC analysis

also shows two ferroic temperatures, Néel and Curie, showing two exothermic peaks at around 370 °C and 830 °C, respectively.

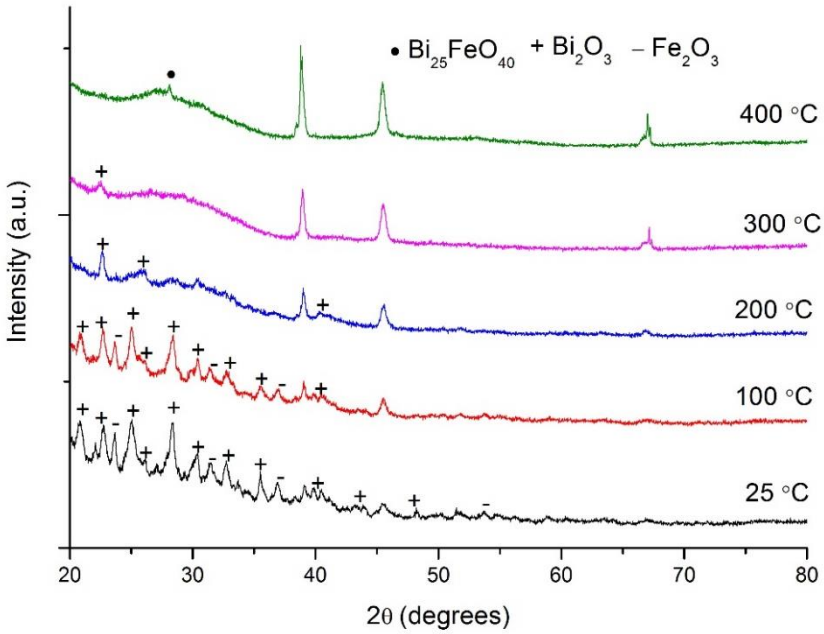

Figure 4.1. In-situ XRD patterns of BFO heated to temperatures in the range of 25 – 400°C.

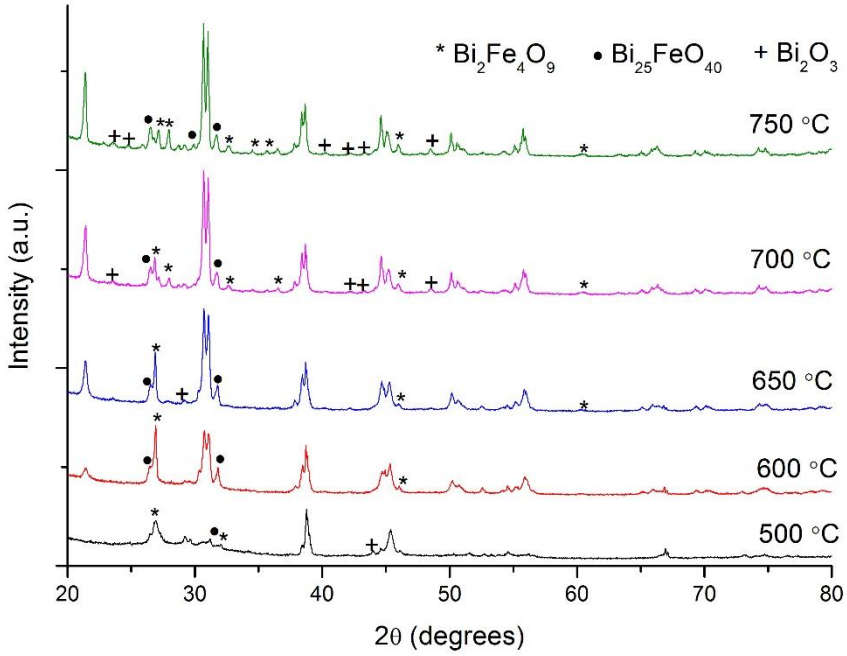

Figure 4.2. In-situ XRD patterns of BFO heated to temperatures in the range of 500 - 750 °C.

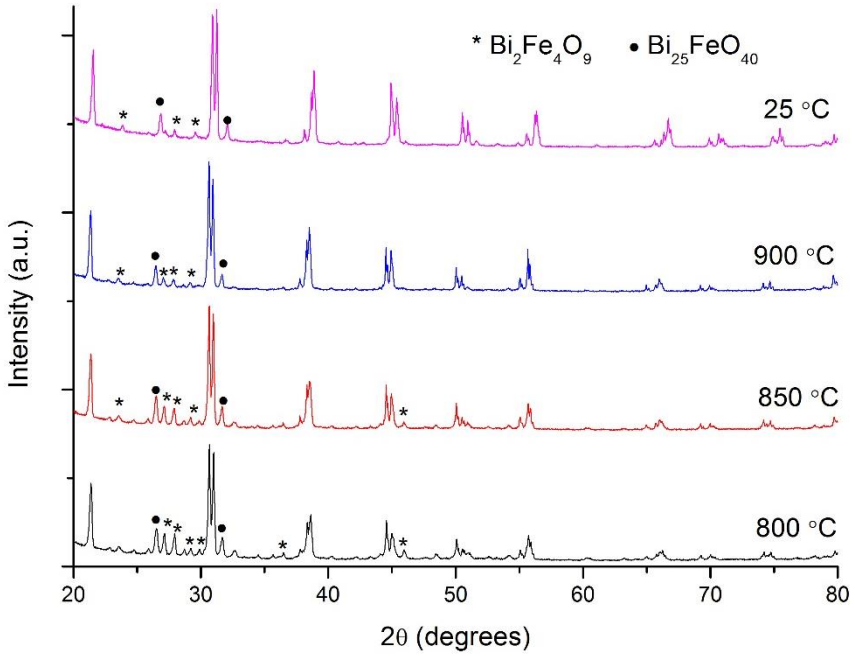

Figure 4.3. In-situ XRD patterns of BFO heated to temperatures in the range of 800 – 900 °C and cooled naturally to room temperature (25 °C).

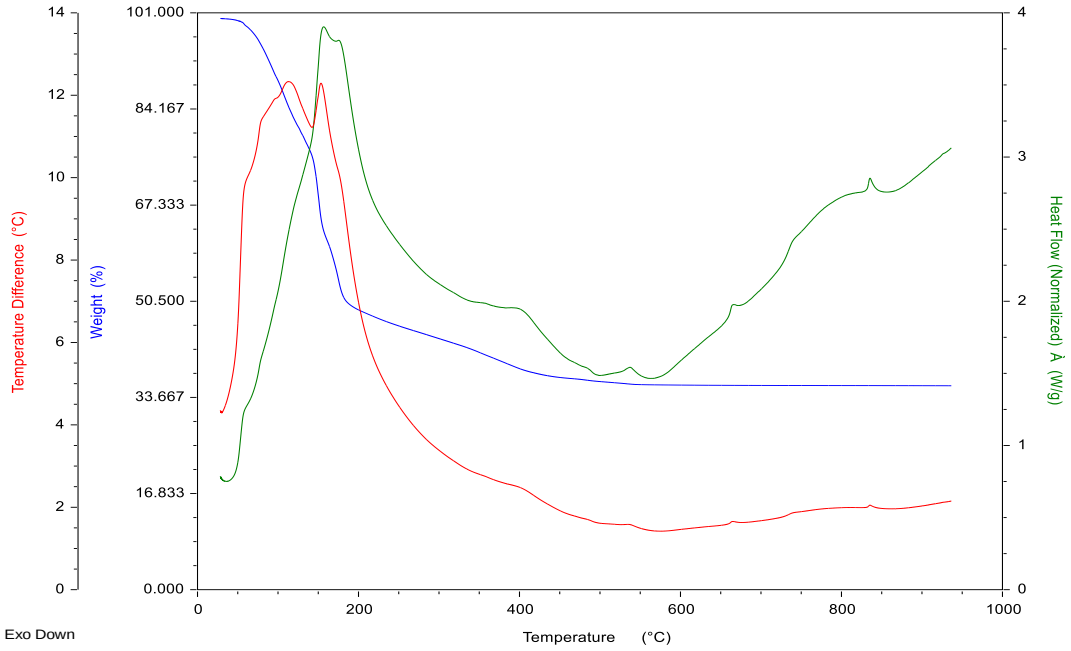

Figure 4.4. A simultaneous thermal analysis (DTA/DSC/TGA) of bismuth ferrite powders heated from 25 to 950 °C.

Since solid state method does not provide a controlled phase transformation and requires a higher reaction temperature, hydrothermal method was selected as the synthesis method for BFO. To understand how process parameters in hydrothermal method affects the evolution of BFO, various bismuth ferrite particles were synthesized in 4, 8 and 12 M KOH concentration at a fixed set of condition *i.e.*, 200 °C and 20 h. The molarities of KOH in the solution were determined in line with literature values [81]. The corresponding XRD patterns are given in Figure 4.5.

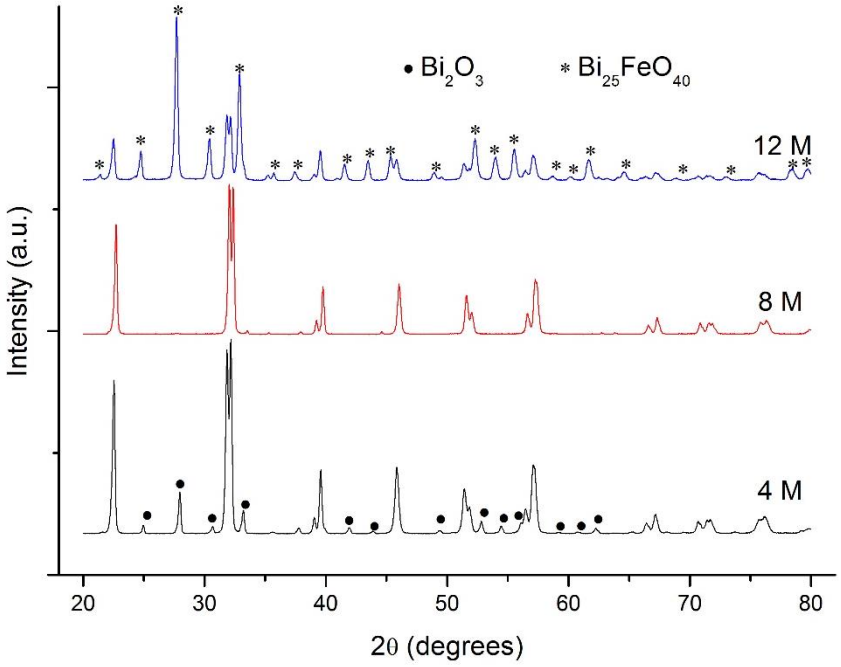

Figure 4.5. XRD patterns of BFO hydrothermally produced with various molarities at a fixed set of condition *i.e.*, 200 °C – 20 h.

All the peaks in BFO produced with 8 M KOH concentration are indexed as a rhombohedral perovskite structure having a space group of R3c (JCPDS No. 86-1518). However, BFO synthesized with 4 and 12 M displays additional peaks coming from secondary phases, Bi_2O_3 (JCPDS No. 74-1375) and $Bi_{25}FeO_{40}$ (JCPDS No. 73-9538), respectively. Therefore, it can be concluded that production of BFO via a hydrothermal method requires certain KOH concentration. As mineralizer is acting as a bridging agent between the reactants in the solution, lower KOH concentration

is not enough to complete a reaction between $Fe(OH)_3$ and $Bi(OH)_3$. Therefore, residual bismuth hydroxide is then transformed into Bi_2O_3 in the sealed vessel under autogeneous pressure. On the other hand, higher molarity favors the reaction towards the secondary phase of BFO. As a result, KOH concentration plays an important role in the synthesis of BFO via a hydrothermal method.

In case of BFOs synthesized with various reaction durations, all the major peaks are indexed as a rhombohedral phase with a JCPDS number of 86-1518. However, BFO produced at a reaction time of 5 h and 20 h shows additional peaks corresponding to $Bi_{25}FeO_{40}$ having a JCPDS number of 73-9538. Under the light of these information, it can be interpreted that if temperature and molarity are properly fixed, then reaction time does not prominently affect the evolution of BFO.

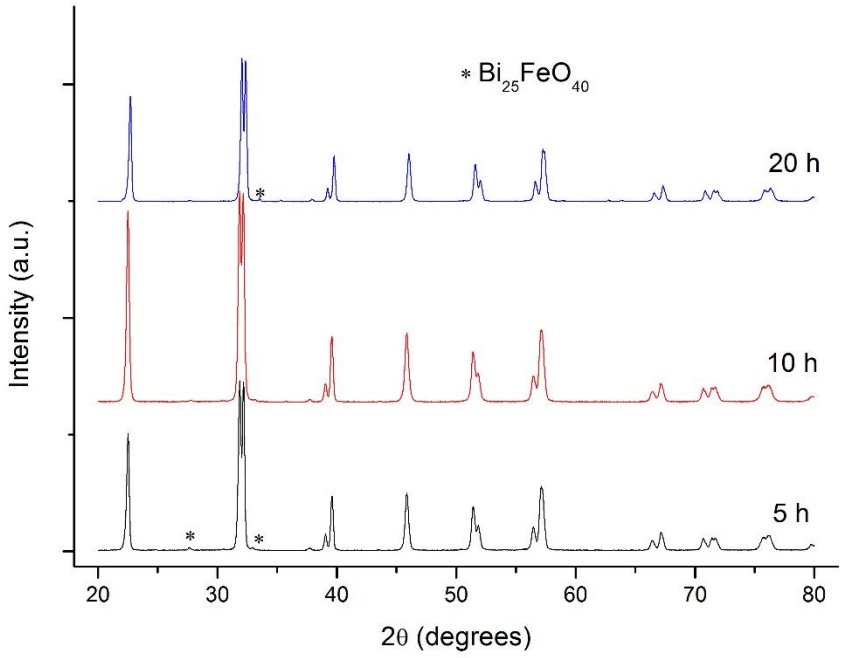

Figure 4.6. XRD patterns of BFO hydrothermally produced with various durations at a fixed set of condition *i.e.*, 200 °C – 8 M.

Apart from duration and molarity of mineralizer, temperature is another key factor affecting phase formation in the hydrothermal synthesis of bismuth ferrites. Since Bi and Fe hydroxides are attacked by KOH mineralizer to dissolve and precipitated in

the solution, which is called as dissolution – crystallization process, temperature and pressure in the enclosed vessel play a crucial role for the crystal growth of supersaturated solution. Figure 4.7 represents different BFO powders produced at various reaction temperatures at a fixed set of condition *i.e.*, 8 M – 10 h. All major peaks are ascribed to rhombohedral BFO phase in addition to adjacent peaks of secondary or impurity phases, in which JCPDS numbers of β-Bi_2O_3, Fe_2O_3, $Bi_{25}FeO_{40}$ and $Bi_{24}(Bi_{1.04}Fe_{0.84})O_{40}$ are 77-5341, 33-0664, 73-9538 and 82-1316, respectively. Higher reaction temperature drives the decomposition of BFO to its secondary phases and initial oxides. On the other hand, evolution of BFO from its hydroxides in the solution does not successfully complete at lower temperatures. Therefore, fabrication at 200 °C having a steam pressure of ca. 200 psi in the vessel may be the best solution in the hydrothermal treatment of BFO.

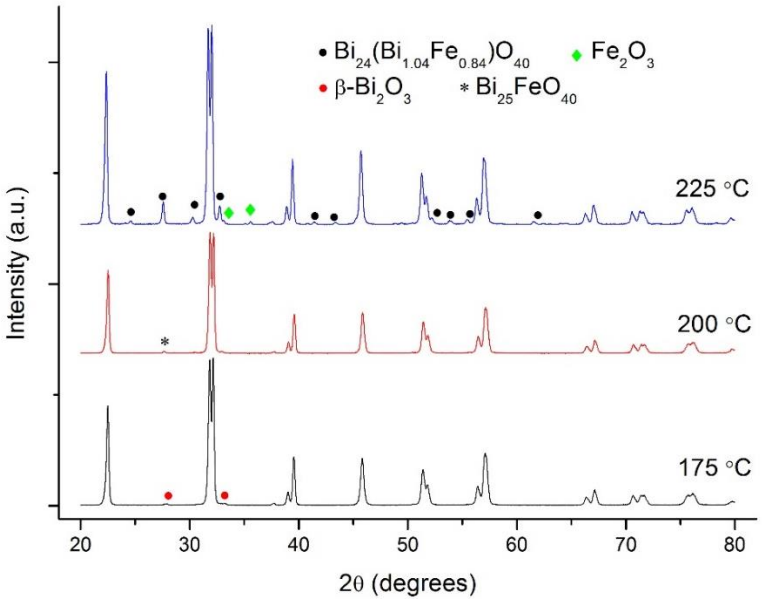

Figure 4.7. XRD patterns of BFO hydrothermally produced at various temperatures at a fixed set of condition *i.e.*, 8 M – 10 h.

4.2 Synthesis of Yb-doped BFOs

Figure 4.8 (a) demonstrates X-ray diffraction (XRD) patterns of BFO and Yb-doped BFOs (BYb1FO, BYb3FO, BYb5FO, BYb10FO) synthesized at 200 °C for 10 h.

These patterns confirmed that all the peaks can be indexed to single phase $BiFeO_3$ having a space group R3c with rhombohedral perovskite structure (JCPDS No. 86-1518) up to 3 at% Yb-doped BFO. After this point, BYb5FO and BYb10FO include presence of secondary phases, $Bi_{25}FeO_{40}$ (JCPDS No. 73-9538) and $Bi_2Fe_4O_9$ (JCPDS No. 25-0090), respectively. It should be noticed that no other phases associated with Yb can be discerned, indicating that doping with Yb formed a solid solution rather than formation of its phase. In addition, incorporation of Yb into BFO creates a slight shift to the right for characteristic twin peaks [(104) and (110)] especially in BYb10FO compared to BFO seen in Figure 4.8 (b). This may arise from the fact that radius of Yb^{3+} (0.0958 nm) ions is smaller than that of Bi^{3+} (0.117 nm), resulting in smaller d spacing. According to Bragg's equation ($n\lambda=2d\sin\theta$), diffraction angle is shifted to the right. Moreover, the crystallite sizes of all samples were calculated using (110) and (202) planes because of their high intensities and absence of adjacent peaks. According to Scherrer's equation ($t = K\lambda/B\cos\theta$ in which t is particle diameter, K is constant taken as 0.89 for spherical particles, λ wavelength of Cu K_α, B is the FWHM, and θ is the diffraction angle of interested plane), the crystallite sizes for BFO, BYb1FO, BYb3FO, BYb5FO, BYb10FO samples are 25 ± 1, 26 ± 3, 28 ± 2, 21 ± 3 and 27 ± 1 nm, respectively.

Figure 4.9 shows scanning electron microscopy (SEM) images of all samples. As seen from Figure 4.9 (a) to Figure 4.9 (e), all samples except BYb10FO appear in more or less cuboidal microstructure with sizes varying from 7 μm to submicron levels. However, BYb10FO exhibits two phase morphology, rod-like and cuboidal one as indicated in Figure 4.9 (e). This is consistent with XRD result of BYb10FO seen in Figure 4.8 (a) which shows the presence of two distinct phases, BFO and $Bi_2Fe_4O_9$. On the other hand, higher magnification images of samples, Figure 4.9 (f) to Figure 4.9 (m), indicate that those cuboidals possess subparticles with different sizes. Irregularity of those particles raises with the increase in Yb content. Moreover, presence of Yb^{3+} influentially decreases the size of those subparticles. This may be ascribed to the substitution of Yb having different radius compared to that of Bi resulting in inhabitation of crystal growth [107]. Presence of this substitute element

within the perovskite structure may act as an obstruction for particles to grow further, hence, the lowest particle size was achieved in case of BYb10FO.

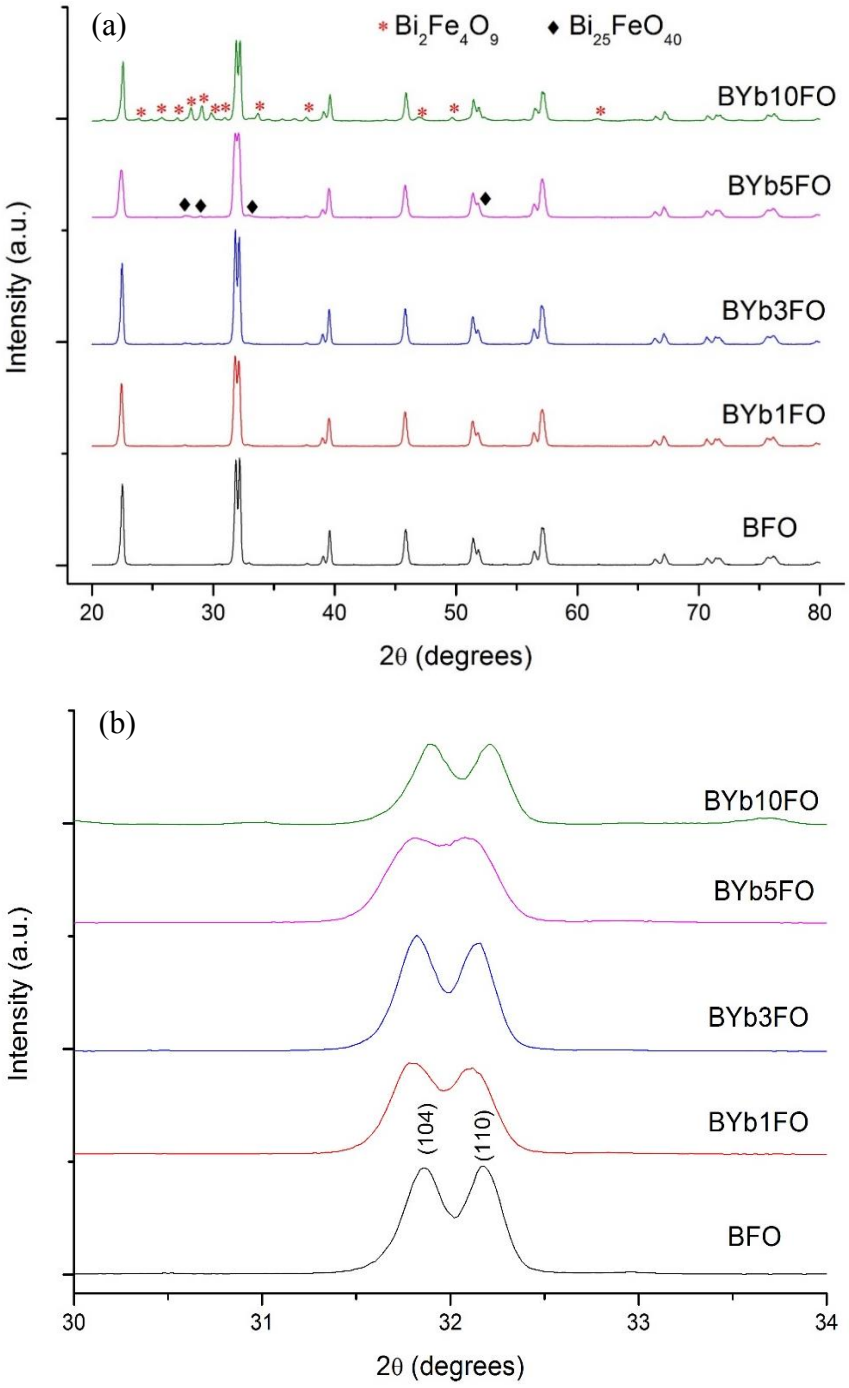

Figure 4.8. (a) XRD patterns of BFO and Yb-doped BFOs. (b) Enlarged view of XRD patterns between the angles of 30°-34°.

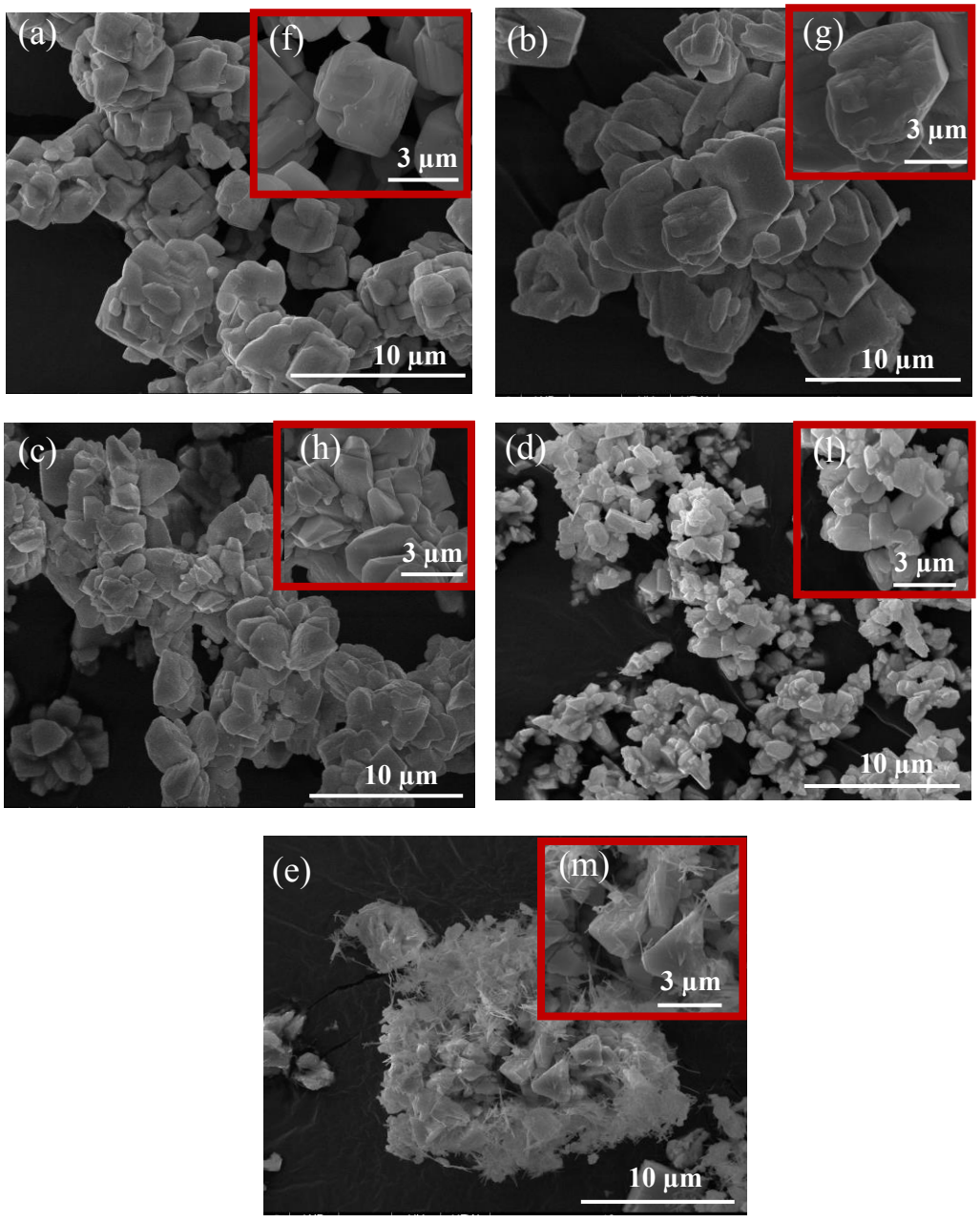

Figure 4.9. SEM images of (a) BFO, (b) BYb1FO, (c) BYb3FO, (d) BYb5FO, (e) BYb10FO. The insets from (f) to (m) present corresponding magnified SEM images of each sample.

XPS measurements were performed on all samples to characterize chemical state of elements together with the effect of dopant on oxygen vacancy concentration in the doped samples. Figure 4.10, 4.11, 4.12 and 4.13 reveal survey spectra of all samples containing Bi, Fe, O and Yb, respectively. All peaks of undoped and Yb-doped BFOs were fitted on Shirley type background and corrected using adventitious C1s binding energy at 284.8 eV. In Figure 4.10, undoped BFO shows a doublet located at 158.8 eV and 164.1 eV with a splitting energy of 5.3 eV, corresponding to the core lines of $4f_{7/2}$ and $4f_{5/2}$ of Bi^{3+}, respectively [108]. However, upon addition of Yb into perovskite structure, these binding energy values of Bi^{3+} are lowered to 158.2 eV and 163.5 eV compared to undoped BFO. This may be a result of substitution of Yb^{3+} with Bi^{3+} reducing binding energy value of Bi 4f [109].

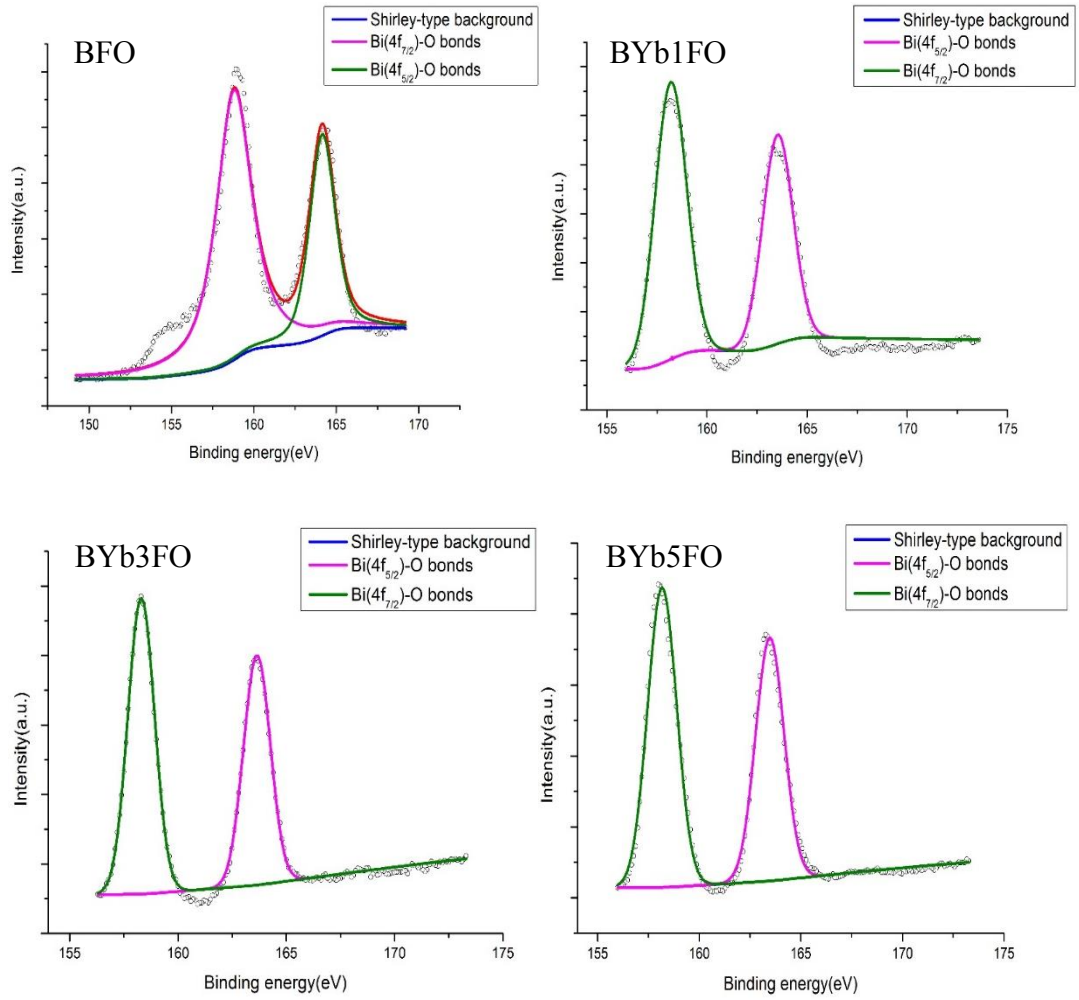

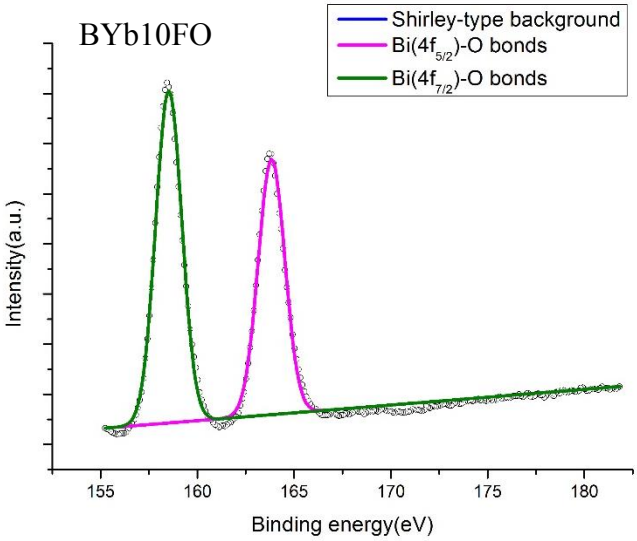

Figure 4.10. XPS spectra of Bi 4f of all samples.

Figure 4.11 presents fitted narrow scan spectra of Fe 2p peaks for all samples. Peaks observed at 710.9 eV and 724.2 eV are assigned to Fe $2p_{3/2}$ and Fe $2p_{1/2}$, mainly ascribing to Fe-O bonds. Spin-orbit splitting energy (Δ) of the pure Fe 2p doublet is 13.3 eV which is comparable with theoretical value of 13.6 eV for Fe_2O_3 [110]. Almost no shift in binding energy values in Fe 2p is one of the evidence of substitution of Yb with Bi rather than Fe.

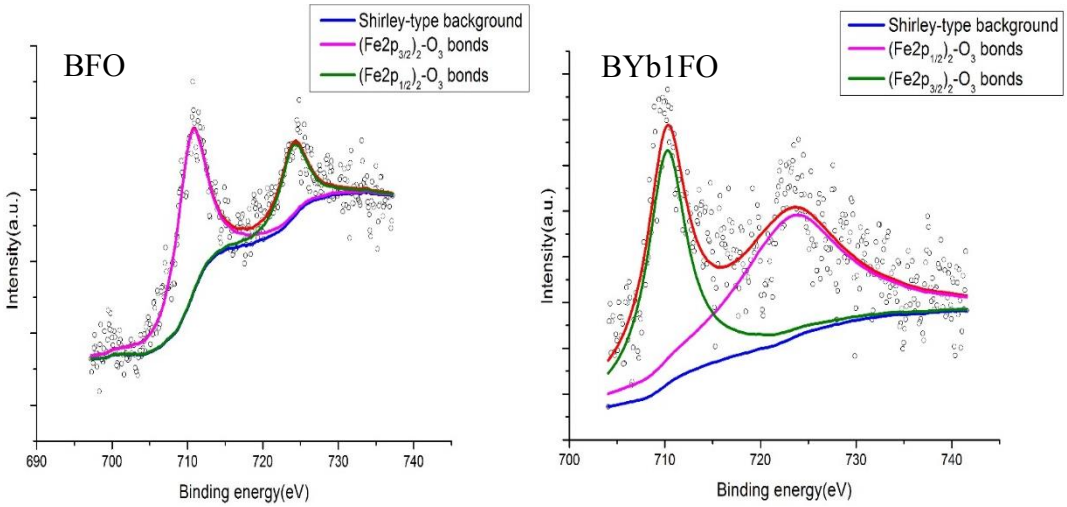

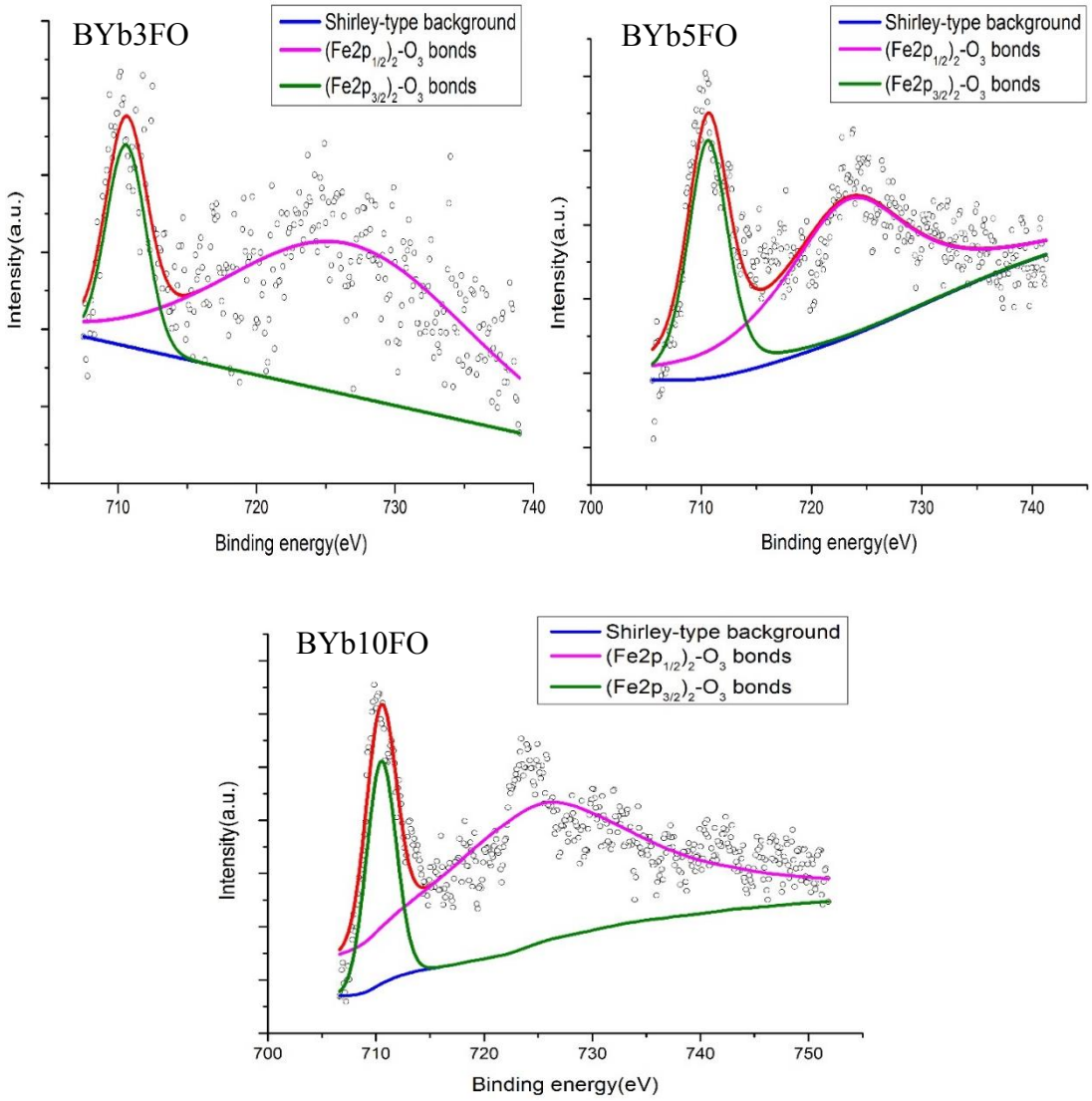

Figure 4.11. XPS spectra of Fe 2p of all samples.

Furthermore, Figure 4.12 and Figure 4.13 display the deconvoluted XPS spectra of Yb 4d and O 1s in doped BFOs. In the former one, peak located at 183.8 eV is assigned to Yb 4d, whose state is attributed to Yb_2O_3 [111]. The latter one represents the core level of O 1s in which two subpeaks are corresponding to the oxygen in the lattice (M-O-M), denoted as O_I, at around 529 eV and to the bonded oxygen species at around 531 eV, denoted as O_{II}, such as oxygen deficiencies, absorbed H_2O on the surface or hydroxyl species [112].

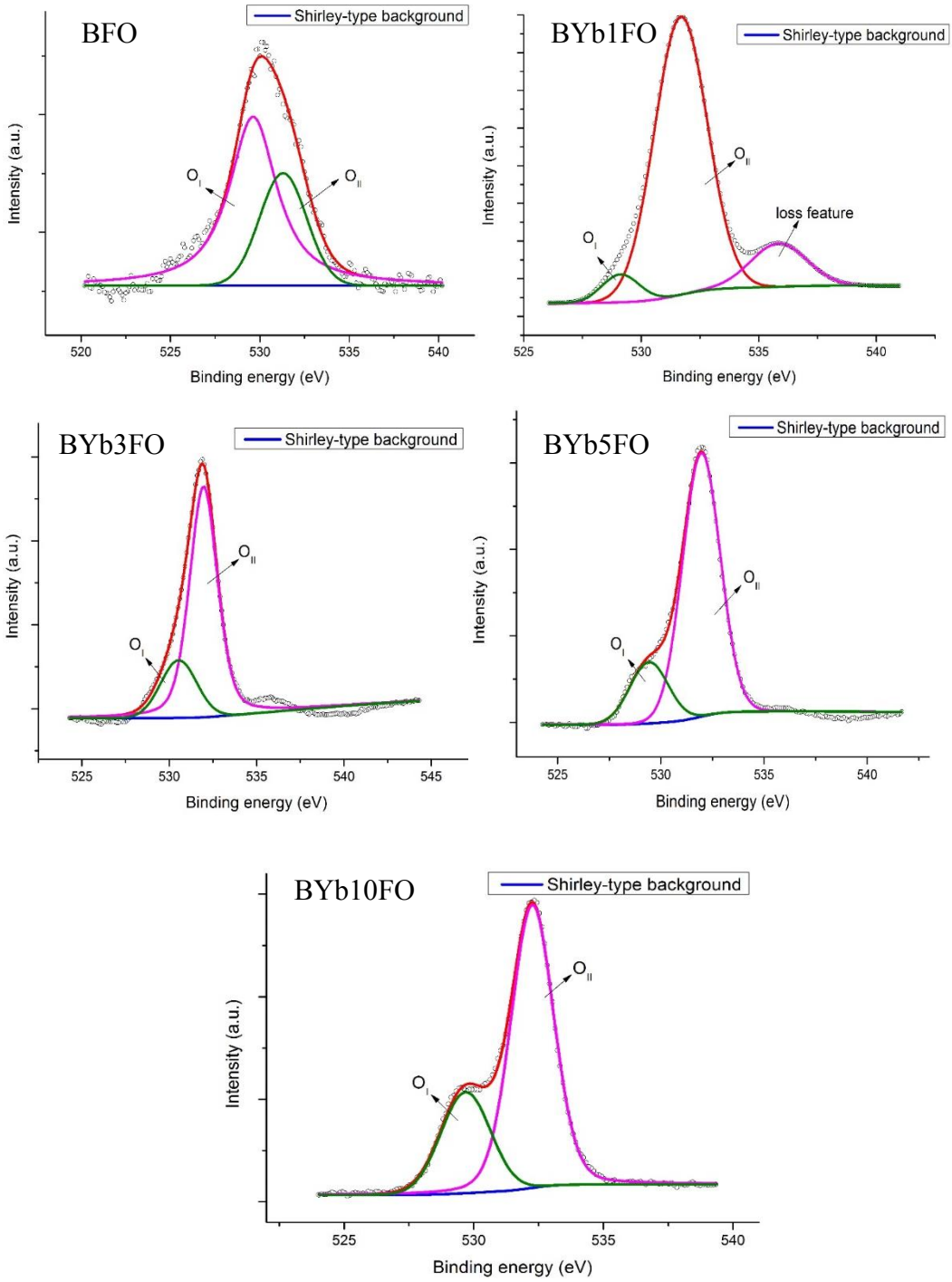

Figure 4.12. XPS spectra of O 1s of all samples.

To elucidate the effect of dopant on the oxygen deficiencies, the area associated with the oxygen in the lattice (O_I) is divided by the area associated with the bonded oxygen species (O_{II}). For convenience, this term is abbreviated as O_I/O_{II} and

corresponding areas are determined using XPS Peak 4.1 programme. This ratio of O_I/O_{II} for Yb-doped BFOs is shown in Table 4.1. It is concluded from this ratio that oxygen content in the lattice is raised dramatically from 7.04% to 39.97% in doped BFOs upon addition of Yb. This may be linked with the formation of more M-O-M bonds with increasing Yb content and reduced oxygen deficiencies [109].

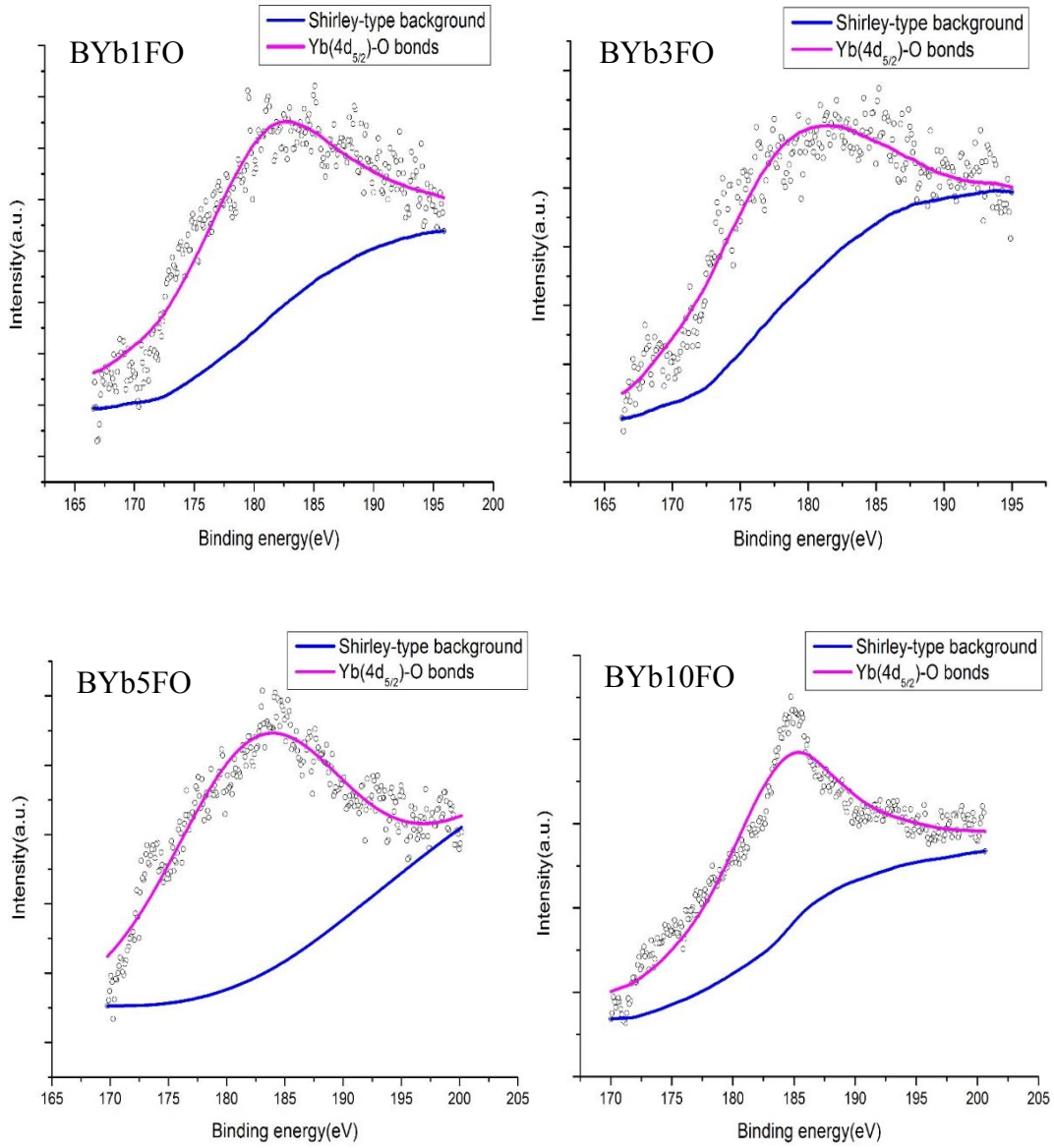

Figure 4.13. XPS spectra of Yb 4d of all samples.

Table 4.1 Ratio of O_I/O_{II} for Yb-doped BFOs.

Sample	O_I/O_{II}
BYb1FO	7.04
BYb3FO	17.32
BYb5FO	22.97
BYb10FO	39.97

Figure 4.14 shows enlarged view of DSC curves of all samples in the temperature range between 700 and 900 °C. As seen in Figure 4.14, pure BFO displays a sharp exothermic peak at 835.5 °C corresponding to its Curie temperature (T_C), which is comparable with the literature value [113]. Upon addition of Yb into perovskite structure, Curie temperature is gradually shifted to lower temperature from 835.5 to 802.6 °C, for BFO and BYb10FO, respectively. However, BYb10FO exhibits a wider peak at its T_C. This may result from compositional fluctuation as a result of presence of secondary phase in BYb10FO [114]. Decrease of T_C with dopant may be attributed to tolerance factor (t) of BFO having a perovskite type of structure (ABO_3) proposed by Goldschmidt [115], which can be expressed as

$$t = \frac{[(1-x)R_{Bi} + xR_{Yb}] + R_O}{\sqrt{2}\,(R_{Fe} + R_O)}$$

where x is the atomic fraction and R is the effective ionic radius of element. Based on the effective ionic radius values and the coordination numbers (12 for Bi^{3+}, 6 for both Fe^{3+} and Yb^{3+}) [116], the tolerance factors calculated for BFO, BYb1FO, BYb3FO, BYb5FO and BYb10FO are 0.961, 0.959, 0.956, 0.952 and 0.944, respectively. Since unity value of t stands for an ideal perovskite cubic structure, deviation from unity results in distortion and change in polarizability within the structure, which in turn affects the Curie temperature of the material [117].

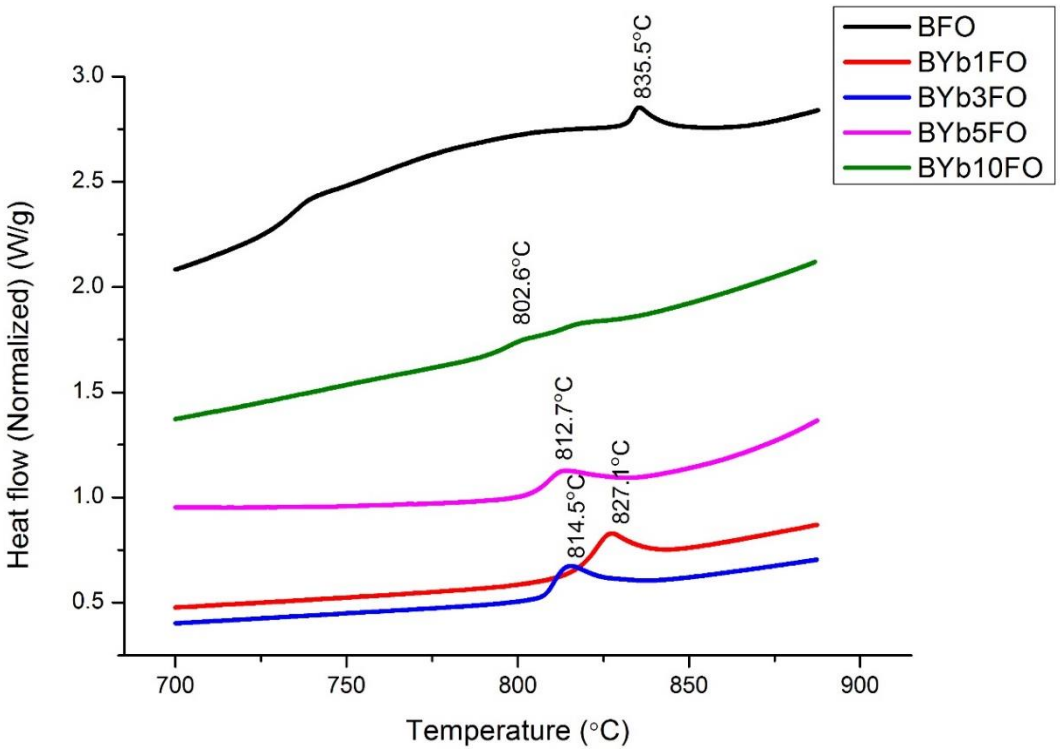

Figure 4.14. Differential scanning calorimeter (DSC) curves of all samples highlighting their Curie temperatures.

Figure 4.15 (a) reveals the room temperature magnetization measurements of BFO and Yb-doped BFOs as a function of applied magnetic field in the range of ±10000 Oe (1 T). Figure 4.15 (b) shows M-H loop in the lower magnetic field range. The hysteresis curve for undoped BFO represents an antiferromagnetic behavior since the loops are not saturated even at high Oe values and almost a linear dependence is observed. However, Yb-doped samples exhibit deviation from linearity and saturation with the high magnetic field of 10 kOe, indicating the weak ferromagnetic behavior. The highest saturation magnetization values for BFO, BYb1FO, BYb3FO, BYb5FO and BYb10FO samples are 0.052, 0.040, 0.090, 0.047 and 0.038 emu/g, respectively. All the other magnetic properties together with P_r values are summarized in Table 4.2. These results clearly indicate that the highest saturation magnetization value is attained in the sample doped with 3 at% Yb in BFO (M_s = 0.090 emu/g) and this value is enhanced by 73% compared to undoped BFO (M_s = 0.052 emu/g). This improvement in the saturation magnetization upon

Yb-doping may be attributed to reduction of the spin cycloid structure in the range of 21-28 nm, where a period length of 64 nm was found in the literature [7]. Reduced size destroys the spin spiral structure and tends to form a better ferromagnetic alignment within the perovskite structure. Park *et al.* investigated this reduced size effect on the magnetic properties of BFO and concluded that saturation magnetization values could be enhanced with decreasing particle sizes [52]. Moreover, as tolerance factor (t) proposes large structural distortion by incorporation of Yb into BFO perovskite structure, this magnetically active Yb^{3+} ions may be more predominant to contribute overall magnetization of BFO, thereby, enhance magnetic properties of BFOs [118].

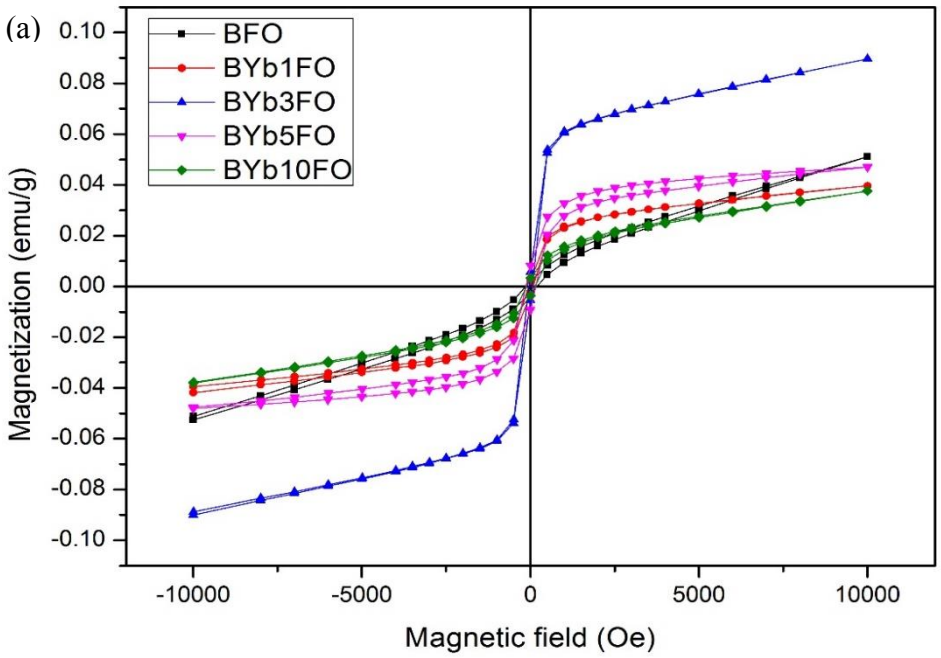

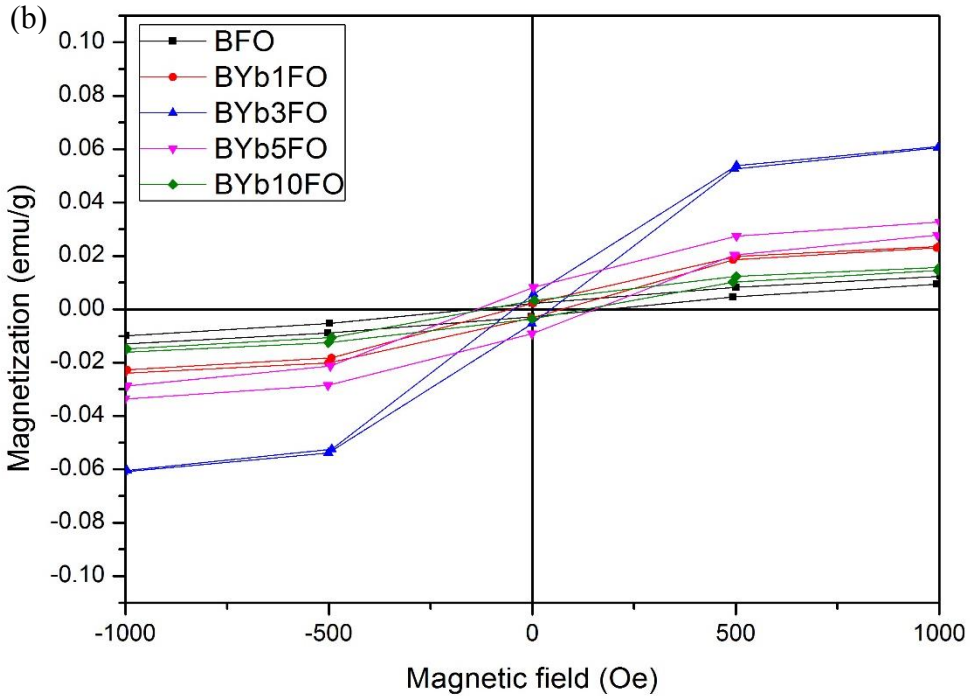

Figure 4.15. (a) Room temperature magnetic measurements of BFO and Yb-doped BFOs. (b) The enlarged view shows low magnetic field range.

Table 4.2 Saturation magnetization (M_s), remanent magnetization (M_r), coercivity (H_c) and remanent polarization (P_r) of Yb-doped BFO series.

Sample	*M_s (emu/g)*	*M_r (emu/g)*	*H_c (Oe)*	*P_r ($\mu C/cm^2$)*
BFO	0.052	0.002	186	0.28
BYb1FO	0.040	0.003	73	0.19
BYb3FO	0.090	0.005	45	0.37
BYb5FO	0.047	0.008	151	0.08
BYb10FO	0.038	0.003	127	0.01

Figure 4.16 shows the ferroelectric hysteresis loop for undoped BFO and Yb-doped BFO series measured at room temperature at a frequency of 10 Hz under the applied voltage of 50 kV/cm. All samples display cigar shaped/circular loop type ferroelectric hysteresis behavior without saturation, indicating the presence of

leakage current. This phenomena is related with oxygen deficiencies within the samples as calculated from XPS spectra, using O_I/O_{II} ratio. As Ederer *et al.* indicated the presence of oxygen vacancies has a detrimental effect on the magnetoelectric properties of multiferroic bismuth ferrite [119], upon addition of Yb, O_I/O_{II} is greatly raised, therefore, it is expected that the lowest leakage current could be present in BYb10FO. Remanent polarization (P_r) values for BFO, BYb1FO, BYb3FO, BYb5FO, and BYb10FO samples are tabulated in Table 4.2. Among all samples, BYb3FO exhibits the highest P_r value. This is mainly because doping results in local distortion, changing the polarizability of sample as calculated from t factor [117]. Although larger degree of distortion is generated in BYb5FO and BYb10FO, presence of secondary phases, $Bi_{25}FeO_{40}$ and $Bi_2Fe_4O_9$, could predominantly affect their P_r values in a decreasing manner.

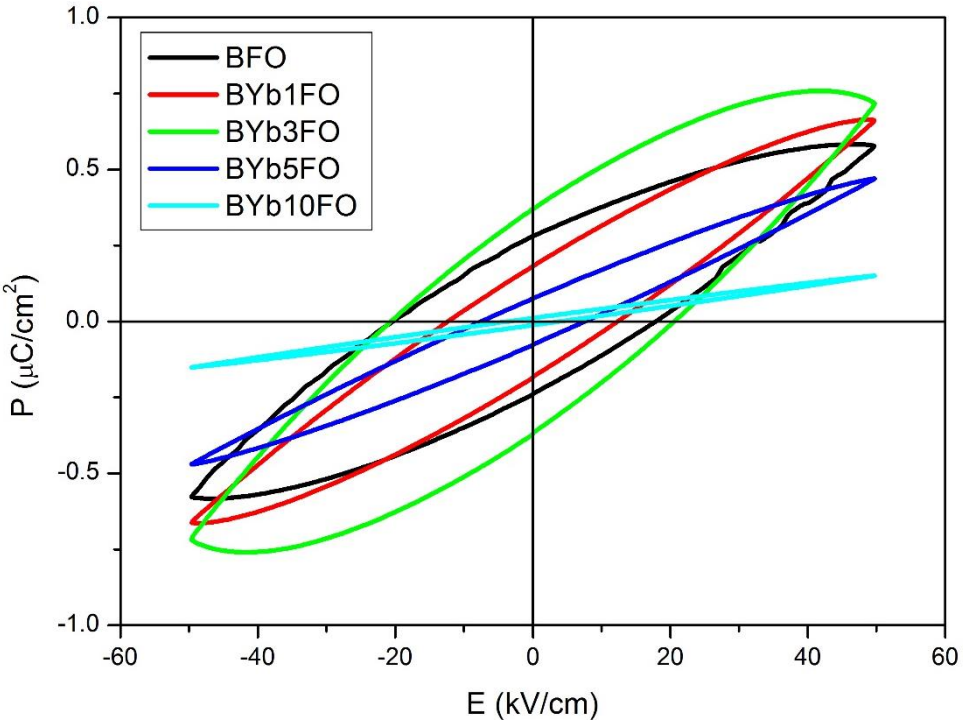

Figure 4.16. Ferroelectric measurements of BFO and Yb-doped BFOs.

Figure 4.17 presents dielectric measurements of all samples as a function of frequency ranging from 20 Hz to 300 kHz at room temperature. The dielectric loss, which is independent of area of pellet, was directly obtained from measurements. On

the other hand, once the measurement system gives parallel capacitance value (C) for each frequency, the dielectric constant (ε_r) was acquired using the formula

$$\varepsilon_r = \frac{tC}{A\varepsilon_0}$$

in which t is pellet thickness, A is the area of pellet, and ε_0 gives permittivity of free space. It is clear from Figure 4.17 (a) that dielectric constant varies differently among all the samples. A significant decrease can be observed in case of BYb3FO, in other words, dielectric constant decreases dramatically with an increase in frequency up to a certain frequency, and then, it becomes constant at higher frequency region. This behavior shows dependence of dielectric constant on applied frequency and presence of higher dielectric loss indicates its lossy dielectric behavior [120]. This behavior is also consistent with corresponding P-E behavior shown in Figure 4.16 due to absence of saturation. Apart from these samples, BYb10FO shows nearly independent dielectric constant behavior on the applied frequency. In other words, in the lower frequency region, the space charges are able to follow the applied electrical field, whereas at higher frequency, these space charges cannot find enough time to orient themselves to follow applied field. Doping may reduce the number of defects within the structure *i.e.*, oxygen vacancy concentration given in XPS section, which in turn, enhances the formation of M-O-M bonds *i.e.*, Bi-O-Bi, Yb-O-Yb and/or Bi-O-Yb. This contributes to attain higher dielectric constant at higher frequency region particularly seen in BYb10FO [121]. Figure 4.17 (b) depicts dielectric loss as a function of frequency up to 300 kHz. Again, higher dielectric loss, or higher energy dissipation, together with lower dielectric constant is another indicative of lossy dielectric behavior for BYb3FO. BYb10FO exhibits the lowest dielectric loss among all samples because oxygen deficiencies are greatly reduced as calculated from XPS spectra.

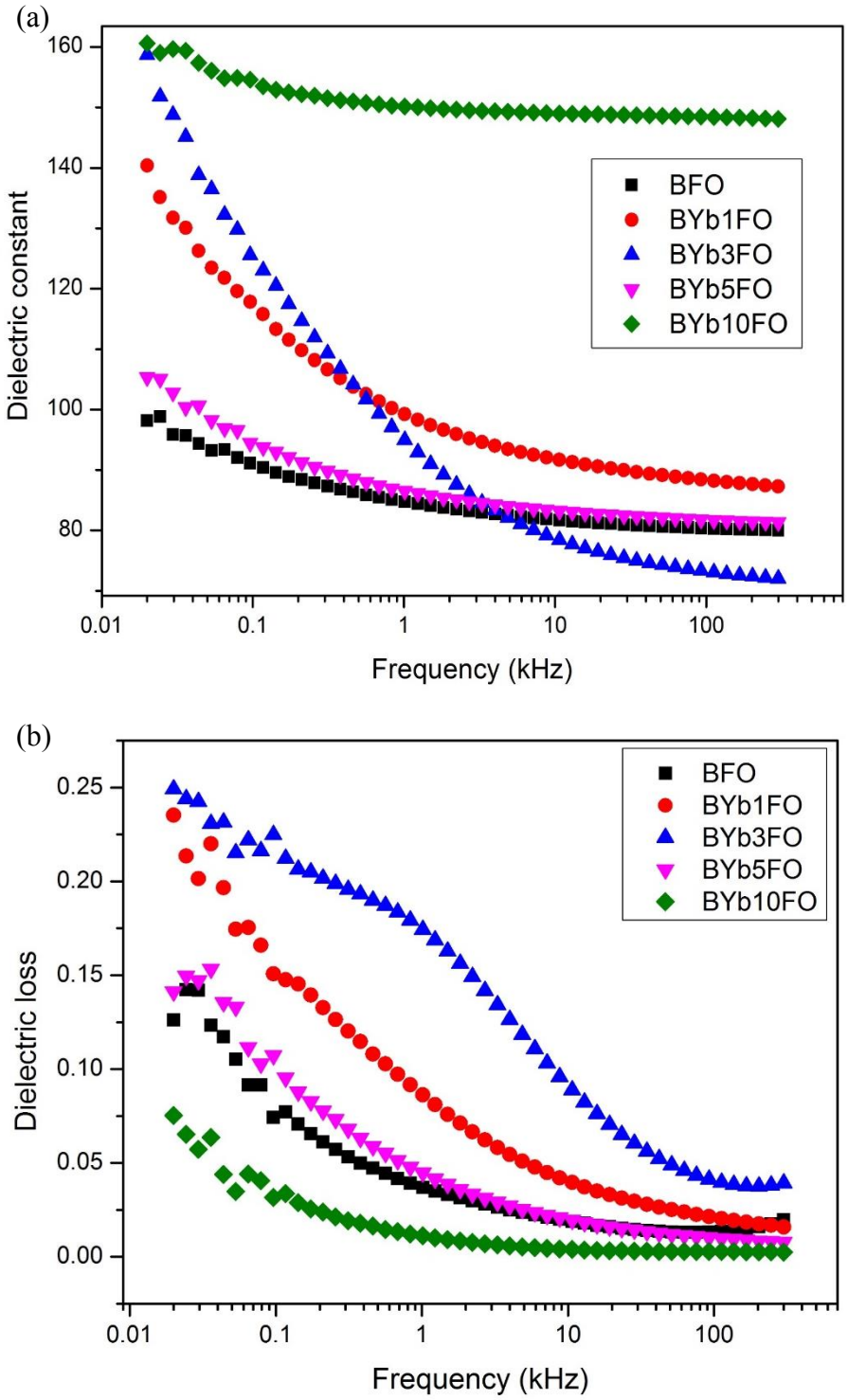

Figure 4.17. Frequency dependent (a) dielectric constant and (b) dielectric loss of BYbFO series measured at room temperature.

CHAPTER 5

CONCLUSIONS AND FUTURE WORK

In this study, understanding of optimum synthesis parameters and doping with Yb into bismuth ferrite perovskite structure through a hydrothermal method were accomplished.

In the first part of the work, undoped BFO particles were produced using the enclosed stainless steel in various conditions. It was observed that KOH concentration in the solution acts as a bridging agent between Bi and Fe hydroxides and drives the formation of BFO under certain molarity. On the other hand, reaction duration did not strongly influence the reaction kinetics as almost all the peaks were indexed to rhombohedral perovskite structure having R3c space group. Besides time and molarity of mineralizer, reaction temperature in the vessel played a crucial role in the phase formation of particles since the status of supersaturated solution predominantly altered the dynamics of dissolution – crystallization process.

In the second part of the work, $Bi_{1-x}Yb_xFeO_3$ (x = 0, 0.01,0.03, 0.05, 0.1) particles were successfully synthesized using a hydrothermal method at 200 °C for 10 h. XRD patterns indicated that incorporation of Yb did not change the crystal structure and all samples showed a distorted rhombohedral perovskite structure. FESEM images demonstrated that powders consisted of subparticles with various sizes. Substitution of Yb reduces the crystallite size of particles, as a result, spiral spin structure becomes modified. In other words, the period length of 64 nm is greatly reduced to the range of 21-28 nm. This reduction enhances magnetic characteristics of Yb-doped BFOs *i.e.*, the highest saturation magnetization value is obtained as 0.090 emu/g in case of BYb3FO. Moreover, tolerance factor, t, calculations indicated that lattice was distorted with the introduction of smaller Yb^{3+} ions into BFO, leading to a change in the polarizability. Similarly, the highest remanent polarization value was

attained as 0.37 μC/cm^2 for BYb3FO. The lattice distortion also affected Curie temperature of Yb-doped bismuth ferrites varying between the temperature ranges of 802.6– 835.5 °C. Dielectric measurements, on the other hand, showed importance of O_I/O_{II} ratio in which BYb10FO exhibited the lowest dielectric loss among other samples.

These results provide new insights into the understanding of effect of rare earth dopant on multiferroic properties of BFO synthesized by hydrothermal method. However, there is still considerable amount of leakage current in the prepared pellets as the ferroelectric hysteresis curve did not show any saturation point. Therefore, a densification process may be applied to overcome the porosity problem in the ceramic pellets. Moreover, incorporation with magnetically active elements such as Co, Mn, Ni for Fe sites may also employed on the ytterbium doped bismuth ferrite powders further to enhance multiferroic properties.

REFERENCES

[1] H. Schmid, "Multi-ferroic magnetoelectrics," *Ferroelectrics*, vol. 162, no. 1, pp. 317–338, 1994.

[2] D. Sando *et al.*, "Crafting the magnonic and spintronic response of $BiFeO_3$ films by epitaxial strain," *Nat. Mater.*, vol. 12, no. 7, pp. 641–646, 2013.

[3] Z. Wang *et al.*, "Highly Sensitive Flexible Magnetic Sensor Based on Anisotropic Magnetoresistance Effect," *Adv. Mater.*, vol. 28, no. 42, pp. 9370–9377, 2016.

[4] J. F. Scott, "Data storage: Multiferroic memories," *Nat. Mater.*, vol. 6, no. 4, pp. 256–257, 2007.

[5] J. Wang *et al.*, "Epitaxial $BiFeO_3$ multiferroic thin film heterostructures," *Science*, vol. 299, no. 5613, pp. 1719–1722, 2003.

[6] S. M. Selbach, T. Tybell, M. A. Einarsrud, and T. Grande, "The ferroic phase transitions of $BiFeO_3$," *Adv. Mater.*, vol. 20, no. 19, pp. 3692–3696, 2008.

[7] S. R. Burns *et al.*, "Expansion of the spin cycloid in multiferroic $BiFeO_3$ thin films," *npj Quantum Mater.*, vol. 4, no. 1, pp. 1–8, 2019.

[8] D. Khomskii, "Classifying multiferroics: Mechanisms and effects," *Physics (College. Park. Md).*, vol. 2, 2009.

[9] H. Maleki, M. Zakeri, and R. Fathi, "Experimental study of the effect of yttrium on the structural, thermal, and magnetic properties of $BiFeO_3$," *Appl. Phys. A*, vol. 124, no. 11, pp. 1–6, 2018.

[10] F. Zhang, X. Zeng, D. Bi, K. Guo, and Y. Yao, "Dielectric, ferroelectric, and magnetic properties of Sm-doped $BiFeO_3$ ceramics prepared by a modified solid-state-reaction method," *Materials (Basel).*, vol. 11, no. 11, 2018.

[11] A. K. Jena, J. A. Chelvane, and J. Mohanty, "Simultaneous improvement of

piezoelectric and magnetic properties in diamagnetic ion modified $BiFeO_3$ film," *J. Alloys Compd.*, vol. 805, pp. 1168–1174, 2019.

[12] Y. Liu *et al.*, "Multiferroic properties of La/Er/Mn/Co multi-doped $BiFeO_3$ thin films," *Ceram. Int.*, vol. 45, no. 9, pp. 11765–11775, 2019.

[13] Y. Wang, Z. Guo, Q. Jia, J. Dong, J. Zhang, and D. Chen, "Effect of Nd/Mn substitution on the structure and magnetic properties of nano-$BiFeO_3$," *J. Alloys Compd.*, vol. 786, pp. 385–393, 2019.

[14] S. Liu, G. Jiang, G. Liu, W. Li, and J. Xing, "Effects of Nd, Al doping on the structure and properties of $BiFeO_3$," *J. Supercond. Nov. Magn.*, vol. 32, no. 2, pp. 261–267, 2019.

[15] Y. W. Lu and X. Qi, "Hydrothermal synthesis of pure and Sb-doped $BiFeO_3$ with the typical hysteresis loops of ideal ferroelectrics," *J. Alloys Compd.*, vol. 774, pp. 386–395, 2019.

[16] J. Lu, L. J. Qiao, P. Z. Fu, and Y. C. Wu, "Phase equilibrium of Bi_2O_3-Fe_2O_3 pseudo-binary system and growth of $BiFeO_3$ single crystal," *J. Cryst. Growth*, vol. 318, no. 1, pp. 936–941, 2011.

[17] V. A. Reddy, N. P. Pathak, and R. Nath, "Particle size dependent magnetic properties and phase transitions in multiferroic $BiFeO_3$ nano-particles," *J. Alloys Compd.*, vol. 543, pp. 206–212, 2012.

[18] R. R. Awasthi, K. Asokan, and B. Das, "Effect of molar concentration on structural, magnetic domain and optical properties of $BiFeO_3$ thin films," *Appl. Phys. A*, vol. 125, no. 5, pp. 1–14, 2019.

[19] S. H. Han *et al.*, "Synthesis and characterization of multiferroic $BiFeO_3$ powders fabricated by hydrothermal method," *Ceram. Int.*, vol. 36, no. 4, pp. 1365–1372, 2010.

[20] X. Xu *et al.*, "Control of crystal phase and morphology in hydrothermal synthesis of $BiFeO_3$ crystal," *J. Cryst. Growth*, vol. 437, pp. 42–48, 2016.

[21] T. Gholam *et al.*, "An experimental study of the local electronic structure of B-site gallium doped bismuth ferrite powders," *Phys. Lett. Sect. A Gen. At. Solid State Phys.*, vol. 381, no. 29, pp. 2367–2373, 2017.

[22] T. Gholam *et al.*, "Local electronic structure analysis of Zn-doped $BiFeO_3$ powders by X-ray absorption fine structure spectroscopy," *J. Alloys Compd.*, vol. 710, pp. 843–849, 2017.

[23] L. Guo and Z. Zhou, "Hydrothermal synthesis and magnetic properties of multiferroic $RMn_{0.5}Fe_{0.5}O_3$ (R = Tb, Dy, and Ho)," *J. Magn. Magn. Mater.*, vol. 458, no. 3, pp. 164–170, 2018.

[24] F. L. Wang *et al.*, "Enhanced magnetic, ferroelectric and optical properties of Sr and Co co-doped $BiFeO_3$ powders," *J. Alloys Compd.*, vol. 810, pp. 1–6, 2019.

[25] P. Tang, D. Kuang, S. Yang, and Y. Zhang, "Hydrothermal synthesis and the structural, morphologic and magnetic characteristics of Mn doped bismuth ferrite crystallites," *J. Mater. Sci. Mater. Electron.*, vol. 27, no. 3, pp. 2594–2600, 2016.

[26] T. Zheng and J. Wu, "Effects of site engineering and doped element types on piezoelectric and dielectric properties of bismuth ferrite lead-free ceramics," *J. Mater. Chem. C*, vol. 3, no. 43, pp. 11326–11334, 2015.

[27] Z. Yan, K. F. Wang, J. F. Qu, Y. Wang, Z. T. Song, and S. L. Feng, "Processing and properties of Yb-doped $BiFeO_3$ ceramics," *Appl. Phys. Lett.*, vol. 91, no. 8, pp. 1–4, 2007.

[28] S. Ahmad, M. A. Khan, M. Sarfraz, A. ur Rehman, M. F. Warsi, and I. Shakir, "The impact of Yb and Co on structural, magnetic, electrical and photocatalytic behavior of nanocrystalline multiferroic $BiFeO_3$ particles," *Ceram. Int.*, vol. 43, no. 18, pp. 16880–16887, 2017.

[29] S. D. Lakshmi and I. B. S. Banu, "Multiferroism and magnetoelectric coupling

in single-phase Yb and X (X = Nb, Mn, Mo) co-doped $BiFeO_3$ ceramics," *J. Sol-Gel Sci. Technol.*, vol. 89, no. 3, pp. 713–721, 2019.

[30] C. Wu, J. Wei, and F. Kong, "Effect of rare earth dopants on the morphologies and photocatalytic activities of $BiFeO_3$ microcrystallites," *J. Mater. Sci. Mater. Electron.*, vol. 24, no. 5, pp. 1530–1535, 2013.

[31] P. Curie, "Sur la symétrie dans les phénomènes physiques, symétrie d'un champ électrique et d'un champ magnétique," *J. Phys. Théorique Appliquée*, vol. 3, no. 1, pp. 393–415, 1894.

[32] I. E. Dzyaloshinskii, "On the magneto-electrical effect in antiferromagnets," *J. Sov. Phys. Jetp*, vol. 10, no. 3, pp. 628–629, 1960.

[33] D. N. Astrov, "The magnetoelectric effect in antiferromagnetics," *Sov. Phys. - JETP*, vol. 11, no. 3, p. 708, 1960.

[34] S. Dong, J. M. Liu, S. W. Cheong, and Z. Ren, "Multiferroic materials and magnetoelectric physics: Symmetry, entanglement, excitation, and topology," *Adv. Phys.*, vol. 64, no. 5–6, pp. 519–626, 2015.

[35] E. Ascher, H. Rieder, H. Schmid, and H. Stössel, "Some properties of ferromagnetoelectric nickel-iodine boracite, $Ni_3B_7O_{13}I$," *J. Appl. Phys.*, vol. 37, no. 3, pp. 1404–1405, 1966.

[36] W. Eerenstein, N. D. Mathur, and J. F. Scott, "Multiferroic and magnetoelectric materials," *Nature*, vol. 442, no. 7104, pp. 759–765, 2006.

[37] D. I. Khomskii, "Coupled electricity and magnetism in solids: Multiferroics and beyond," *Multiferroic Mater. Prop. Tech. Appl.*, pp. 1–31, 2016.

[38] Y. J. Choi, H. T. Yi, S. Lee, Q. Huang, V. Kiryukhin, and S. W. Cheong, "Ferroelectricity in an ising chain magnet," *Phys. Rev. Lett.*, vol. 100, no. 4, pp. 6–9, 2008.

[39] D. V. Efremov, J. Van Den Brink, and D. I. Khomskii, "Bond- versus site-

centred ordering and possible ferroelectricity in manganites," *Nat. Mater.*, vol. 3, no. 12, pp. 853–856, 2004.

[40] N. Hur, S. Park, P. A. Sharma, J. S. Ahn, S. Guha, and S. W. Cheong, "Electric polarization reversal and memory in a multiferroic material induced by magnetic fields," *Nature*, vol. 429, no. 6990, pp. 392–395, 2004.

[41] A. J. C. Buurma, G. R. Blake, and T. T. M. Palstra, *Multiferroic Materials: Physics and Properties*. Elsevier Ltd., 2016.

[42] I. A. Sergienko and E. Dagotto, "Role of the Dzyaloshinskii-Moriya interaction in multiferroic perovskites," *Phys. Rev. B - Condens. Matter Mater. Phys.*, vol. 73, pp. 1–5, 2006.

[43] T. Kimura, J. C. Lashley, and A. P. Ramirez, "Inversion-symmetry breaking in the noncollinear magnetic phase of the triangular-lattice antiferromagnet $CuFeO_2$," *Phys. Rev. B - Condens. Matter Mater. Phys.*, vol. 73, no. 22, pp. 1–4, 2006.

[44] I. A. Sergienko, C. Şen, and E. Dagotto, "Ferroelectricity in the magnetic E-phase of orthorhombic perovskites," *Phys. Rev. Lett.*, vol. 97, no. 22, pp. 3–6, 2006.

[45] J. M. Moreau, C. Michel, R. Gerson, and W. J. James, "Ferroelectric $BiFeO_3$ X-ray and neutron diffraction study," *J. Phys. Chem. Solids*, vol. 32, no. 6, pp. 1315–1320, 1971.

[46] F. Kubel and H. Schmid, "Structure of a ferroelectric and ferroelastic monodomain crystal of the perovskite $BiFeO_3$," *Acta Crystallogr. Sect. B*, vol. 46, no. 6, pp. 698–702, 1990.

[47] Y. H. Chu, L. W. Martin, M. B. Holcomb, and R. Ramesh, "Controlling magnetism with multiferroics," *Mater. Today*, vol. 10, no. 10, pp. 16–23, 2007.

[48] I. Sosnowska, T. P. Neumaier, and E. Steichele, "Spiral magnetic ordering in

bismuth ferrite," *J. Phys. C Solid State Phys.*, vol. 15, no. 23, pp. 4835–4846, 1982.

[49] J. R. Teague, R. Gerson, and W. J. James, "Dielectric hysteresis in single crystal $BiFeO_3$," *Solid State Commun.*, vol. 8, no. 13, pp. 1073–1074, 1970.

[50] J. T. Heron, D. G. Schlom, and R. Ramesh, "Electric field control of magnetism using $BiFeO_3$-based heterostructures," *Appl. Phys. Rev.*, vol. 1, no. 2, pp. 0–18, 2014.

[51] D. Lebeugle, D. Colson, A. Forget, M. Viret, A. M. Bataille, and A. Gukasov, "Electric-field-induced spin flop in $BiFeO_3$ single crystals at room temperature," *Phys. Rev. Lett.*, vol. 100, no. 22, pp. 1–4, 2008.

[52] T. J. Park, G. C. Papaefthymiou, A. J. Viescas, A. R. Moodenbaugh, and S. S. Wong, "Size-dependent magnetic properties of single-crystalline multiferroic $BiFeO_3$ nanoparticles," *Nano Lett.*, vol. 7, no. 3, pp. 766–772, 2007.

[53] T. J. Park, Y. Mao, and S. S. Wong, "Synthesis and characterization of multiferroic $BiFeO_3$ nanotubes," *Chem. Commun.*, no. 23, pp. 2708–2709, 2004.

[54] R. Palai *et al.*, "β phase and γ-β metal-insulator transition in multiferroic $BiFeO_3$," *Phys. Rev. B - Condens. Matter Mater. Phys.*, vol. 77, no. 1, pp. 1–11, 2008.

[55] G. Xu, H. Hiraka, G. Shirane, J. Li, J. Wang, and D. Viehland, "Low symmetry phase in (001) $BiFeO_3$ epitaxial constrained thin films," *Appl. Phys. Lett.*, vol. 86, no. 18, pp. 1–3, 2005.

[56] D. Ricinschi, K. Y. Yun, and M. Okuyama, "A mechanism for the 150 μC cm^{-2} polarization of $BiFeO_3$ films based on first-principles calculations and new structural data," *J. Phys. Condens. Matter*, vol. 18, no. 6, pp. L97–L105, 2006.

[57] L. Yan, H. Cao, J. Li, and D. Viehland, "Triclinic phase in tilted (001) oriented

$BiFeO_3$ epitaxial thin films," *Appl. Phys. Lett.*, vol. 94, no. 13, pp. 15–18, 2009.

[58] G. L. Yuan, S. W. Or, J. M. Liu, and Z. G. Liu, "Structural transformation and ferroelectromagnetic behavior in single-phase $Bi_{1-x}Nd_xFeO_3$ multiferroic ceramics," *Appl. Phys. Lett.*, vol. 89, no. 5, 2006.

[59] M. H. Lee *et al.*, "High-performance lead-free piezoceramics with high Curie temperatures," *Adv. Mater.*, vol. 27, no. 43, pp. 6976–6982, 2015.

[60] M. Valant, A. K. Axelsson, and N. Alford, "Peculiarities of a solid-state synthesis of multiferroic polycrystalline $BiFeO_3$," *Chem. Mater.*, vol. 19, no. 22, pp. 5431–5436, 2007.

[61] S. M. Selbach, M. A. Einarsrud, T. Tybell, and T. Grande, "Synthesis of $BiFeO_3$ by wet chemical methods," *J. Am. Ceram. Soc.*, vol. 90, no. 11, pp. 3430–3434, 2007.

[62] D. Maurya, H. Thota, K. S. Nalwa, and A. Garg, "$BiFeO_3$ ceramics synthesized by mechanical activation assisted versus conventional solid-state-reaction process: A comparative study," *J. Alloys Compd.*, vol. 477, no. 1–2, pp. 780–784, 2009.

[63] J. Silva, A. Reyes, H. Esparza, H. Camacho, and L. Fuentes, "$BiFeO_3$: A review on synthesis, doping and crystal structure," *Integr. Ferroelectr.*, vol. 126, no. 1, pp. 47–59, 2011.

[64] H. Ke *et al.*, "Factors controlling pure-phase multiferroic $BiFeO_3$ powders synthesized by chemical co-precipitation," *J. Alloys Compd.*, vol. 509, no. 5, pp. 2192–2197, 2011.

[65] A. Palewicz, R. Przeniosło, I. Sosnowska, and A. W. Hewat, "Atomic displacements in $BiFeO_3$ as a function of temperature: Neutron diffraction study," *Acta Crystallogr. Sect. B Struct. Sci.*, vol. 63, no. 4, pp. 537–544, 2007.

[66] V. A. Khomchenko *et al.*, "Effect of diamagnetic Ca, Sr, Pb, and Ba substitution on the crystal structure and multiferroic properties of the $BiFeO_3$ perovskite," *J. Appl. Phys.*, vol. 103, no. 2, 2008.

[67] H. Han, J. H. Lee, and H. M. Jang, "Low-temperature solid-state synthesis of high-purity $BiFeO_3$ ceramic for ferroic thin-film deposition," *Inorg. Chem.*, vol. 56, no. 19, pp. 11911–11916, 2017.

[68] J. Wu, S. Mao, Z. G. Ye, Z. Xie, and L. Zheng, "Room-temperature ferromagnetic/ferroelectric $BiFeO_3$ synthesized by a self-catalyzed fast reaction process," *J. Mater. Chem.*, vol. 20, no. 31, pp. 6512–6516, 2010.

[69] M. Ahmadzadeh, A. Ataie, and E. Mostafavi, "The effects of mechanical activation energy on the solid-state synthesis process of $BiFeO_3$," *J. Alloys Compd.*, vol. 622, pp. 548–556, 2015.

[70] K. L. Da Silva *et al.*, "Mechanosynthesized $BiFeO_3$ nanoparticles with highly reactive surface and enhanced magnetization," *J. Phys. Chem. C*, vol. 115, no. 15, pp. 7209–7217, 2011.

[71] N. Nuraje and K. Su, "Perovskite ferroelectric nanomaterials," *Nanoscale*, vol. 5, no. 19, pp. 8752–8780, 2013.

[72] F. Chen *et al.*, "Sol-gel derived multiferroic $BiFeO_3$ ceramics with large polarization and weak ferromagnetism," *Appl. Phys. Lett.*, vol. 89, no. 9, pp. 67–70, 2006.

[73] T. Liu, Y. Xu, and J. Zhao, "Low-temperature synthesis of $BiFeO_3$ via PVA sol-gel route," *J. Am. Ceram. Soc.*, vol. 93, no. 11, pp. 3637–3641, 2010.

[74] Q. Zhang, D. Sando, and V. Nagarajan, "Chemical route derived bismuth ferrite thin films and nanomaterials," *J. Mater. Chem. C*, vol. 4, no. 19, pp. 4092–4124, 2016.

[75] K. S. Suslick, "Sonochemistry," *Science*, vol. 247, no. 4949, pp. 1439–1445, 1990.

[76] J. H. Bang and K. S. Suslick, “Applications of ultrasound to the synthesis of nanostructured materials,” *Adv. Mater.*, vol. 22, no. 10, pp. 1039–1059, 2010.

[77] R. Mazumder *et al.*, “Particle size dependence of magnetization and phase transition near T_N in multiferroic $BiFeO_3$,” *J. Appl. Phys.*, vol. 100, no. 3, 2006.

[78] N. Das, R. Majumdar, A. Sen, and H. S. Maiti, “Nanosized bismuth ferrite powder prepared through sonochemical and microemulsion techniques,” *Mater. Lett.*, vol. 61, no. 10, pp. 2100–2104, 2007.

[79] S. H. Feng and G. H. Li, “Hydrothermal and solvothermal syntheses,” *Modern Inorganic Synthetic Chemistry: Second Edition*, Elsevier, 2017, pp. 73–104.

[80] G. Demazeau, “Solvothermal and hydrothermal processes: The main physico-chemical factors involved and new trends,” *Res. Chem. Intermed.*, vol. 37, no. 2–5, pp. 107–123, 2011.

[81] C. Chen, J. Cheng, S. Yu, L. Che, and Z. Meng, “Hydrothermal synthesis of perovskite bismuth ferrite crystallites,” *J. Cryst. Growth*, vol. 291, no. 1, pp. 135–139, 2006.

[82] X. Z. Chen, Z. C. Qiu, J. P. Zhou, G. Zhu, X. B. Bian, and P. Liu, “Large-scale growth and shape evolution of bismuth ferrite particles with a hydrothermal method,” *Mater. Chem. Phys.*, vol. 126, no. 3, pp. 560–567, 2011.

[83] J. T. Han *et al.*, “Tunable synthesis of bismuth ferrites with various morphologies,” *Adv. Mater.*, vol. 18, no. 16, pp. 2145–2148, 2006.

[84] S. Li, Y. H. Lin, B. P. Zhang, Y. Wang, and C. W. Nan, “Controlled fabrication of $BiFeO_3$ uniform microcrystals and their magnetic and photocatalytic behaviors,” *J. Phys. Chem. C*, vol. 114, no. 7, pp. 2903–2908, 2010.

[85] J. Prado-Gonjal, M. E. Villafuerte-Castrejón, L. Fuentes, and E. Morán,

"Microwave-hydrothermal synthesis of the multiferroic $BiFeO_3$," *Mater. Res. Bull.*, vol. 44, no. 8, pp. 1734–1737, 2009.

[86] U. A. Joshi, J. S. Jang, P. H. Borse, and J. S. Lee, "Microwave synthesis of single-crystalline perovskite $BiFeO_3$ nanocubes for photoelectrode and photocatalytic applications," *Appl. Phys. Lett.*, vol. 92, no. 24, pp. 2006–2009, 2008.

[87] X. Zhu *et al.*, "Microwave hydrothermal synthesis, structural characterization, and visible-light photocatalytic activities of single-crystalline bismuth ferric nanocrystals," *J. Am. Ceram. Soc.*, vol. 94, no. 8, pp. 2688–2693, 2011.

[88] A. R. Makhdoom, S. M. Shah, T. Mahmood, M. J. Iqbal, M. J. Akhtar, and M. A. Rafiq, "Enhancement of ferromagnetism by suppression of spiral spin structure in Ba doped $BiFeO_3$," *J. Magn. Magn. Mater.*, vol. 484, pp. 286–290, 2019.

[89] Y. Ahn and J. Y. Son, "Multiferroic properties and ferroelectric domain structures of Yb-doped $BiFeO_3$ thin films on glass substrates," *Phys. B Condens. Matter*, vol. 558, no. November 2018, pp. 24–27, 2019.

[90] Z. Chen, J. Hu, Z. Lu, and X. He, "Low-temperature preparation of lanthanum-doped $BiFeO_3$ crystallites by a sol-gel-hydrothermal method," *Ceram. Int.*, vol. 37, no. 7, pp. 2359–2364, 2011.

[91] M. Arora, S. Chauhan, P. C. Sati, and M. Kumar, "Effect of non-magnetic ions substitution on structural, magnetic and optical properties of $BiFeO_3$ nanoparticles," *J. Supercond. Nov. Magn.*, vol. 27, no. 8, pp. 1867–1871, 2014.

[92] J. Khajonrit, N. Prasoetsopha, T. Sinprachim, P. Kidkhunthod, S. Pinitsoontorn, and S. Maensiri, "Structure, characterization, and magnetic/ electrochemical properties of Ni-doped $BiFeO_3$ nanoparticles," *Adv. Nat. Sci. Nanosci. Nanotechnol.*, vol. 8, no. 1, p. 015010, 2017.

[93] S. Basu, S. K. M. Hossain, D. Chakravorty, and M. Pal, "Enhanced magnetic properties in hydrothermally synthesized Mn-doped $BiFeO_3$ nanoparticles," *Curr. Appl. Phys.*, vol. 11, no. 4, pp. 976–980, 2011.

[94] Y. Du, Z. X. Cheng, S. X. Dou, M. Shahbazi, and X. L. Wang, "Enhancement of magnetization and dielectric properties of chromium-doped $BiFeO_3$ with tunable morphologies," *Thin Solid Films*, vol. 518, pp. e5–e8, 2010.

[95] M. Kumar and K. L. Yadav, "Study of room temperature magnetoelectric coupling in Ti substituted bismuth ferrite system," *J. Appl. Phys.*, vol. 100, no. 7, pp. 1–5, 2006.

[96] Q. Xu, H. Zai, D. Wu, T. Qiu, and M. X. Xu, "The magnetic properties of $Bi(Fe_{0.95}Co_{0.05})O_3$ ceramics," *Appl. Phys. Lett.*, vol. 95, no. 11, pp. 2012–2015, 2009.

[97] Y. K. Jun *et al.*, "Effects of Nb-doping on electric and magnetic properties in multi-ferroic $BiFeO_3$ ceramics," *Solid State Commun.*, vol. 135, no. 1–2, pp. 133–137, 2005.

[98] S. K. Pradhan, "Influence of iron deficiency on electric and magnetic behavior of Ho doped $BiFeO_3$ electroceramic," *J. Mater. Sci. Mater. Electron.*, vol. 24, no. 5, pp. 1720–1726, 2013.

[99] P. Tang, D. Kuang, S. Yang, and Y. Zhang, "Structural, morphological and multiferroic properties of the hydrothermally grown gadolinium (Gd) and manganese (Mn) doped sub-micron bismuth ferrites," *J. Alloys Compd.*, vol. 656, pp. 912–919, 2016.

[100] X. J. Xi *et al.*, "Modulation of electric conduction in La-Mg codoped multiferroic $BiFeO_3$ ceramics," *J. Alloys Compd.*, vol. 603, pp. 224–229, 2014.

[101] P. C. Sati, M. Arora, S. Chauhan, M. Kumar, and S. Chhoker, "Structural, magnetic, vibrational and impedance properties of Pr and Ti codoped $BiFeO_3$

multiferroic ceramics," *Ceram. Int.*, vol. 40, no. 6, pp. 7805–7816, 2014.

[102] M. A. Basith, O. Kurni, M. S. Alam, B. L. Sinha, and B. Ahmmad, "Room temperature dielectric and magnetic properties of Gd and Ti co-doped $BiFeO_3$ ceramics," *J. Appl. Phys.*, vol. 115, no. 2, 2014.

[103] J. S. Park, Y. J. Yoo, J. S. Hwang, J. H. Kang, B. W. Lee, and Y. P. Lee, "Enhanced ferromagnetic properties in Ho and Ni co-doped $BiFeO_3$ ceramics," *J. Appl. Phys.*, vol. 115, no. 1, 2014.

[104] J. Xu *et al.*, "Enhanced dielectric and multiferroic properties of single-phase y and Zr co-doped $BiFeO_3$ ceramics," *J. Appl. Phys.*, vol. 114, no. 15, pp. 0–5, 2013.

[105] R. Castañeda *et al.*, "Effects of Ni doping on ferroelectric and ferromagnetic properties of $Bi_{0.75}Ba_{0.25}FeO_3$," *Ceram. Int.*, vol. 39, no. 7, pp. 8527–8530, 2013.

[106] C. Lan, Y. Jiang, and S. Yang, "Magnetic properties of La and (La, Zr) doped $BiFeO_3$ ceramics," *J. Mater. Sci.*, vol. 46, no. 3, pp. 734–738, 2011.

[107] G. S. Arya and N. S. Negi, "Effect of In and Mn co-doping on structural, magnetic and dielectric properties of $BiFeO_3$ nanoparticles," *J. Phys. D. Appl. Phys.*, vol. 46, no. 9, 2013.

[108] R. Das, T. Sarkar, and K. Mandal, "Multiferroic properties of Ba^{2+} and Gd^{3+} co-doped bismuth ferrite: Magnetic, ferroelectric and impedance spectroscopic analysis," *J. Phys. D. Appl. Phys.*, vol. 45, no. 45, 2012.

[109] Z. Guo *et al.*, "Solution-processed ytterbium oxide dielectrics for low-voltage thin-film transistors and inverters," *Ceram. Int.*, vol. 43, no. 17, pp. 15194–15200, 2017.

[110] J. F. Moulder, W. F. Stickle, P. E. Sobol, and K. D. Bomben, *Handbook of X-ray photoelectron spectroscopy*. 1992.

[111] J. Reszczyńska *et al.*, "Visible light activity of rare earth metal doped (Er^{3+}, Yb^{3+} or Er^{3+}/Yb^{3+}) titania photocatalysts," *Appl. Catal. B Environ.*, vol. 163, pp. 40–49, 2015.

[112] J. Zemek, J. Houdkova, P. Jiricek, T. Izak, and M. Kalbac, "Non-destructive depth profile reconstruction of single-layer graphene using angle-resolved X-ray photoelectron spectroscopy," *Appl. Surf. Sci.*, vol. 491, no. January, pp. 16–23, 2019.

[113] D. Carranza-Celis *et al.*, "Control of multiferroic properties in $BiFeO_3$ nanoparticles," *Sci. Rep.*, vol. 9, no. 1, pp. 1–9, 2019.

[114] N. Petnoi, P. Bomlai, S. Jiansirisomboon, and A. Watcharapasorn, "Effects of Nb-doping on the micro-structure and dielectric properties of $(Bi_{0.5}Na_{0.5})TiO_3$ ceramics," *Ceram. Int.*, vol. 39, no. SUPPL.1, pp. S113–S117, 2013.

[115] V. M. Goldschmidt, "Die Gesetze der Krystallochemie," *Naturwissenschaften*, vol. 14, no. 1, pp. 477–485, 1926.

[116] R. D. Shannon, "Revised effective ionic radii and systematic studies of interatomic distances in halides and chalcogenides," *Acta Crystallogr. Sect. A*, vol. A32, pp. 751–767, 1976.

[117] H. Shimizu, H. Guo, S. E. Reyes-Lillo, Y. Mizuno, K. M. Rabe, and C. A. Randall, "Lead-free antiferroelectric: $xCaZrO_3$-$(1-x)NaNbO_3$ system ($0 \leq x \leq 0.10$)," *Dalt. Trans.*, vol. 44, no. 23, pp. 10763–10772, 2015.

[118] J. Wei, R. Haumont, R. Jarrier, P. Berhtet, and B. Dkhil, "Nonmagnetic Fe-site doping of $BiFeO_3$ multiferroic ceramics," *Appl. Phys. Lett.*, vol. 96, no. 10, pp. 2008–2011, 2010.

[119] C. Ederer and N. A. Spaldin, "Influence of strain and oxygen vacancies on the magnetoelectric properties of multiferroic bismuth ferrite," *Phys. Rev. B - Condens. Matter Mater. Phys.*, vol. 71, no. 22, pp. 1–9, 2005.

[120] S. O. Leontsev and R. E. Eitel, "Dielectric and piezoelectric properties in Mn-

modified (1-x)$BiFeO_3$-x$BaTiO_3$ ceramics," *J. Am. Ceram. Soc.*, vol. 92, no. 12, pp. 2957–2961, 2009.

[121] K. Chakrabarti *et al.*, "Enhanced magnetic and dielectric properties of Eu and Co co-doped $BiFeO_3$ nanoparticles," *Appl. Phys. Lett.*, vol. 101, no. 4, pp. 1–6, 2012.